REPORT DOCUMENTATION PAGE

The public reporting burden for this collection of information is estimated to average 1 hour per response, including the time for reviewing instructions, searching existing data sources, gathering and maintaining the data needed, and completing and reviewing the collection of information. Send comments regarding this burden estimate or any other aspect of this collection of information, including suggestions for reducing the burden, to Department of Defense, Washington Headquarters Services, Directorate for Information Operations and Reports (0704-0188), 1215 Jefferson Davis Highway, Suite 1204, Arlington, VA 22202-4302. Respondents should be aware that notwithstanding any other provision of law, no person shall be subject to any penalty for failing to comply with a collection of information if it does not display a currently valid OMB control number. **PLEASE DO NOT RETURN YOUR FORM TO THE ABOVE ADDRESS.**

1. REPORT DATE *(DD-MM-YYYY)*	2. REPORT TYPE	3. DATES COVERED *(From - To)*
07-01-2002	Final	01-09-2000 – 20-10-2001

4. TITLE AND SUBTITLE

Optimal Design of Hybrid Composite Flywheel Rotor

5a. CONTRACT NUMBER
F6256200M9212

5b. GRANT NUMBER

5c. PROGRAM ELEMENT NUMBER

6. AUTHOR(S)

Prof. Sung Kyu Ha

5d. PROJECT NUMBER

5e. TASK NUMBER

5f. WORK UNIT NUMBER

7. PERFORMING ORGANIZATION NAME(S) AND ADDRESS(ES)
Hanyang University
Sa1-dong, Ansan-si
Kyungi-do 425-791
Korea (South)

8. PERFORMING ORGANIZATION REPORT NUMBER

N/A

9. SPONSORING/MONITORING AGENCY NAME(S) AND ADDRESS(ES)

AOARD
UNIT 45002
APO AP 96337-5002

10. SPONSOR/MONITOR'S ACRONYM(S)

AOARD

11. SPONSOR/MONITOR'S REPORT NUMBER(S)
AOARD-004009

12. DISTRIBUTION/AVAILABILITY STATEMENT

Approved for public release; distribution is unlimited.

20020129 091

13. SUPPLEMENTARY NOTES

14. ABSTRACT An optimal design procedure for composite flywheel rotors was developed. The composite materials were inherently anisotropic: the mechanical and thermal properties differed with direction, causing large residual stresses to develop during the manufacturing process. Such residual stresses add to mechanical stresses developed during rotation. A model was proposed, which quantitatively characterized the process-induced residual stresses. Cylinders of three sizes were manufactured and the residual strains in the radial and hoop directions were measured. The measured residual stains were then compared with those from the model. The effects of the residual stresses on a hybrid rotor were then analyzed by comparing the two-dimensional solution to the three-dimensional finite-element program. The residual stresses in the rotor with the angle variation along the radial direction were also analyzed. Finally, the stress-analysis module was linked to a program in which the design variables can be optimized for the various sizes and material sequences of the composite flywheel rotor with a consideration of both the residual stresses and the rotational centrifugal stresses.

15. SUBJECT TERMS

Composite Materials, Flywheel Rotor

16. SECURITY CLASSIFICATION OF:

a. REPORT	b. ABSTRACT	c. THIS PAGE	17. LIMITATION OF ABSTRACT	18. NUMBER OF PAGES	19a. NAME OF RESPONSIBLE PERSON
U	U	U	UU	46	Thomas D. Kim

19b. TELEPHONE NUMBER *(Include area code)*
+81-3-5410-4409

Standard Form 298 (Rev. 8/98)

Optimal Design of Hybrid Composite Flywheel Rotor,

Phase I

A Final Report

To

THE AIR FORCE OFFICE OF SCIENTIFIC RESEARCH

Prepared By

Prof. Sung Kyu Ha

Young-Bok Yoon

Dong-Jin Kim

Dept. of Mech. Eng., Hanyang University

January 2002

CONTENTS

1. SUMMARY

An optimal design procedure of the composite flywheel rotor is proposed with a consideration of the residual stresses caused during the manufacturing process. The composite materials are inherently anisotropic: the mechanical and thermal properties differ between the longitudinal and the transverse directions. This anisotropic property makes the composite materials superior to other conventional metal in the design of the flywheel rotor. However, at the same time, the anisotropic properties cause the residual stresses to develop in manufacturing process. The induced residual stresses, especially in the weak radial direction, deteriorate the overall performance of the composite flywheel rotor. The residual stresses in the thick wound composite structure can be as high as the strengths of the rotor. Such residual stresses add to the mechanical stresses developed during the rotational speed, thus limiting its full capability. Therefore, in addition to the mechanical stresses, the residual stresses should be controlled in the manufacturing process and properly taken care of in the design of the rotor. The thorough simulation of the manufacturing process and the residual stresses is extremely difficult since many physical phenomena are involved. In this work, first of all, a simple model has been proposed which quantitatively characterize the process-induced residual stresses using a effective temperature change. The cylinders of three different sizes have been manufactured and the residual strains in the radial and hoop directions are then measured by split-ring method. The measured residual stains have then been predicted and compared with those by the model. The effects of the residual stresses on the hybrid rotor were then analyzed by comparing the two-dimensional solution to the three-dimensional finite element program. The residual stresses in the rotor with the angle variation along the radial direction were also analyzed. Finally, the stress analysis module was linked to an optimization program in which the design variables, e.g., the thickness of each hybrid ring can be optimized for the various size and material sequences of the composite flywheel rotor with a consideration of both the residual stresses and the rotational centrifugal stresses.

2. INTRODUCTION

An advanced composite flywheel has recently attracted the considerable attention of many investigators for many energy storage applications including electric utilities, hybrid or electric vehicles and spacecraft [1-5]. The composite flywheel rotor has characteristics of distinctively high energy density, long life and lightweight. The essential components of a flywheel energy storage system are a composite flywheel rotor, motor/generator, power transforming electronics, magnetic bearing, and housing. Recent efforts in development of the flywheel have been devoted to the experimental and theoretical research on increasing the performance and insuring the safety of the flywheel. It is well known that the rotor strength can be significantly improved by properly adjusting the ply stiffness along the radial direction. Especially, along with technical innovations in high strength composite materials, many investigations have been devoted to increasing the total stored energy (TSE) of the flywheel rotor [6-10]. The approaches for calculating the stress distribution of a hybrid composite rotor subjected to centrifugal forces have been cited in literature [1~10].

During the curing process of the filament wound structure, the residual stresses are developed mostly due to the chemical shrinkage and the thermal expansion. Those residual stresses are very complicatedly affected by the degree of anisotropy, the dimensions of the rotor and the curing temperature cycle [12~16]. The radial tensile stresses developed during the curing process generally deteriorate the energy storage capability since the stresses are additive to the radial tensile stresses which are also developed during the rotation of the rotor. Therefore, the curing stresses have to be reduced as much as possible to increase the energy storage capability. However, the certain level of the curing stresses is indispensable and cannot be completely avoided. Therefore, they have to be considered in the design of the composite flywheel rotor. However, methods for evaluating the effects of material properties and curing residual stress on the energy storage capability have not been pertinently addressed. Moreover, no investigation thus far has addressed how to optimally design the hybrid composite rotor considering both the curing residual stresses and the centrifugal stresses.

In this work, the residual stresses developed during the curing process are modeled

4

as an effective thermal loading, which greatly simplify the calculation of the residual stresses; in this way, only a temperature increase need to be determined. The two-dimensional stress analyses for the flywheel rotor based on the assumptions of plane stress (PSS), plane strain (PSN), and generalized plane strain (GPS) have been developed which consider the material hybridization and the angle variation together with the thermal loading. The two-dimensional analyses are then evaluated using three dimensional finite element methods. Overall it is found that PSS is the best analysis method for the flywheel rotor. The equivalent thermal loading is also estimated using the well-known cure simulation program WINDTHICK [14~16], and it is found that the method is very accurate enough to predict the residual stresses and strains developed during the whole curing process.

An optimal design program (FLYOPT) has been finally developed using the Microsoft Excel interface. In the program, the rotor is divided into as many rings as users define and each thickness and winding angle of the rings can be optimized to maximize the performance of the flywheel rotor, especially the total stored energy.

3. 2-DIMENSIONAL STRESS & STRENGTH ANALYSIS

For a numerical calculation, the composite flywheel rotor of varying material properties is divided into many rings and each ring is assumed to have a constant material property of an angle-ply laminate $[(\pm\phi)_m]$ as shown in Figure 1. Based on the assumption of a generalized plane strain state, all the rings are free to expand or contract in the axial direction but have the same axial strain. The flywheel rotor is also assumed cylindrically orthotropic and subject to axisymmetric centrifugal forces due to rotation. With the axisymmetric conditions, the circumferential displacements are thus neglected. All the displacements and stresses are thus independent of the axial and circumferential directions. The radial equilibrium equation for each ring and the axial force equilibrium equation for the rotor are concurrently solved and expressed in a stiffness matrix with the radial displacements and the uniform axial strain. Once the displacements and the axial strain are obtained, the stresses and strength ratios are calculated for all the rings.

3.1   Stress Analysis

The stress distribution in each ring is governed by the radial equilibrium equation, which is written in cylindrical coordinates as [24]

$$\frac{d\sigma_r}{dr}+\frac{\sigma_r-\sigma_\theta}{r}+\rho r\omega^2=0 \tag{1}$$

where σ_r and σ_θ are the radial and circumferential stresses, respectively, ρ denotes a density, and ω the rotational angular velocity. The stress-strain relation in the cylindrical coordinate system as shown in Figure 1 is written as

$$\sigma = Q(\varepsilon - \alpha\Delta T) = Q\varepsilon - \beta\Delta T \tag{2}$$

where σ and ε are the stress and strain vectors, respectively, Q and α denotes a stiffness matrix and thermal expansion coefficient vector in cylindrical coordinates. Eq. (2) can be rewritten in the cylindrical coordinate system as

$$\begin{pmatrix} \sigma_\theta \\ \sigma_z \\ \sigma_r \\ \sigma_{\theta z} \end{pmatrix} = \begin{bmatrix} Q_{11} & Q_{12} & Q_{13} & Q_{16} \\ Q_{21} & Q_{22} & Q_{23} & Q_{26} \\ Q_{31} & Q_{32} & Q_{33} & Q_{36} \\ Q_{61} & Q_{62} & Q_{63} & Q_{66} \end{bmatrix} \begin{pmatrix} \varepsilon_\theta \\ \varepsilon_z \\ \varepsilon_r \\ \varepsilon_{\theta z} \end{pmatrix} - \begin{pmatrix} \beta_\theta \\ \beta_z \\ \beta_r \\ \beta_{\theta z} \end{pmatrix}\Delta T \tag{3}$$

6

In Eq. (3), the axial stress is zero in a plane stress (PSS) assumption and the axial strain is zero in a plane strain (PSN) assumption. More generally, the axial strain is assumed to be a constant in the generalized plane strain (GPS) assumption. Together with these assumptions, the circumferential and radial strains are expressed by the r-direction displacement u_r:

$$\varepsilon_\theta = \frac{u_r}{r}, \; \varepsilon_r = \frac{\partial u_r}{\partial r}, \; \varepsilon_{\theta z} = 0, \text{ and } \begin{cases} \sigma_z = 0 & \text{PSS} \\ \varepsilon_z = 0 & \text{PSN} \\ \varepsilon_z = \varepsilon_o & \text{GPS} \end{cases} \tag{4}$$

Substituting Eqs. (3) and (4) into Eq. (1) yields the radial displacement u_r:

$$u_r = -\rho\omega^2 \varphi_0 r^3 + C_1 \varphi_1 r^\kappa + C_2 \varphi_2 r^{-\kappa} + \varphi_3 \varepsilon_o r + \varphi_{T1} \Delta T r \tag{5}$$

C_1 and C_2 in Eq. (5) are unknown constants to be determined from the boundary conditions, and κ and φ_i are defined in terms of the material properties:

$$\kappa = \sqrt{\frac{Q_{11}}{Q_{33}}}, \quad \varphi_0 = \frac{1}{(9-\kappa^2)Q_{33}}, \varphi_1 = \frac{1}{Q_{13} + \kappa Q_{33}}$$

$$\varphi_2 = \frac{1}{Q_{13} - \kappa Q_{33}}, \quad \varphi_3 = \frac{Q_{12} - Q_{23}}{Q_{33} - Q_{11}} \text{ and } \varphi_{T1} = \frac{\beta_r - \beta_\theta}{Q_{33} - Q_{11}} \tag{6}$$

Substitution of Eq. (5) into Eqs. (3) and (4) yields

$$\varepsilon_r = -3\rho\omega^2 \varphi_o r^2 + \kappa C_1 \varphi_1 r^{\kappa-1} - \kappa C_2 \varphi_2 r^{-\kappa-1} + \varphi_3 \varepsilon_o + \varphi_{T1} \Delta T \tag{7}$$

$$\sigma_r = -\rho\omega^2 \varphi_4 r^2 + C_1 r^{\kappa-1} + C_2 r^{-\kappa-1} + \varphi_5 \varepsilon_o + \varphi_{T2} \Delta T \tag{8}$$

where

$$\varphi_4 = \frac{3Q_{33} + Q_{13}}{(9-\kappa^2)Q_{33}}, \quad \varphi_5 = (Q_{31} + Q_{33})\varphi_3 + Q_{32} \text{ and } \quad \varphi_{T2} = (Q_{31} + Q_{33})\varphi_{T1} - \beta_r \tag{9}$$

In order to derive the stiffness matrix, the radial displacements at the inner and outer surfaces are written in a displacement vector using Eq. (4),

$$\boldsymbol{u} = \rho\omega^2 \boldsymbol{u}_\omega + \varepsilon_o \boldsymbol{u}_\varepsilon + \Delta T \boldsymbol{u}_T + \boldsymbol{G}\boldsymbol{\Phi}\boldsymbol{C} \tag{10}$$

where

7

$$u - \begin{pmatrix} u_{r_i} \\ u_{r_o} \end{pmatrix}, \quad u_\omega - -\varphi_0 \begin{pmatrix} r_i^3 \\ r_o^3 \end{pmatrix}, \quad u_\varepsilon - \varphi_3 \begin{pmatrix} r_i \\ r_o \end{pmatrix}, \quad u_T - \varphi_{T1} \begin{pmatrix} r_i \\ r_o \end{pmatrix}$$

(11)

$$G - \begin{bmatrix} r_i^\kappa & r_i^{-\kappa} \\ r_o^\kappa & r_o^{-\kappa} \end{bmatrix}, \quad \Phi - \begin{bmatrix} \varphi_1 & 0 \\ 0 & \varphi_2 \end{bmatrix} \text{ and } C - \begin{pmatrix} C_1 \\ C_2 \end{pmatrix}$$

In Eq. (11), r_i denotes the inner radius of a ring, and r_o the outer radius of a ring. The normal radial stresses at those two radii can be also written in a force vector using Eq. (8),

$$f_b = \rho \omega^2 f_\sigma + \varepsilon_o f_\varepsilon + \Delta T f_T + I^* G C$$

(12)

where

$$f_b = \begin{pmatrix} -r_i \sigma_{r_i} \\ r_o \sigma_{r_o} \end{pmatrix}, \quad f_\sigma - -\varphi_4 \begin{pmatrix} -r_i^3 \\ r_o^3 \end{pmatrix}, \quad f_\varepsilon = \varphi_5 \begin{pmatrix} -r_i \\ r_o \end{pmatrix}, \quad f_T = \varphi_{T2} \begin{pmatrix} -r_i \\ r_o \end{pmatrix} \text{ and } I^* = \begin{bmatrix} -1 & 0 \\ 0 & 1 \end{bmatrix}$$ (13)

Eliminating the constants C in Eqs. (10) and (12) derives the relation of stresses and displacements at the inner and outer surface of each ring. The derived equation can be expressed as

$$ku = f_b + \rho \omega^2 f_\omega + \varepsilon_o f_\varepsilon + \Delta T f_T$$

(14)

The ring stiffness matrix k is

$$k = I^* G \Phi^{-1} G^{-1} = \frac{1}{\zeta_2} \begin{bmatrix} \kappa \zeta_1 Q_{33} - \zeta_2 Q_{13} & -2\kappa Q_{33} \\ -2\kappa Q_{33} & \kappa \zeta_1 Q_{33} + \zeta_2 Q_{13} \end{bmatrix}$$

(15)

where

$$\zeta_1 = \zeta^{-\kappa} + \zeta^\kappa, \quad \zeta_2 = \zeta^{-\kappa} - \zeta^\kappa \text{ and } \zeta = \frac{r_i}{r_o}$$

(16)

Notice that, in defining the force term f_b of Eq. (14), the stress component was multiplied by its radius, and the ring stiffness matrix k becomes symmetric. In Eq. (14), f_ω, f_ε and f_T are related to the centrifugal force and defined as

$$f_\omega = \begin{pmatrix} f_{\omega_i} \\ f_{\omega_o} \end{pmatrix} = -f_\sigma + ku_\omega$$

$$f_\varepsilon = \begin{pmatrix} f_{\varepsilon_i} \\ f_{\varepsilon_o} \end{pmatrix} = -f_{\bar{\varepsilon}} + ku_\varepsilon$$

(17)

$$f_T = \begin{pmatrix} f_{\omega_i} \\ f_{\omega_o} \end{pmatrix} = -f_{\bar{T}} + ku_T$$

8

The constant axial strain ε_o in Eq. (14) can be computed from force balance in the axial direction. Since there is no external axial force applied on the top and bottom surfaces, the summation of the axial forces over all the rings should be zero:

$$\sum_{j=1}^{N} 2\pi \int_{r_i^{(j)}}^{r_o^{(j)}} \sigma_z^{(j)} r\,dr = 0 \qquad (18)$$

Using the expressions of σ_z in Eq. (3), and u_r and ε_r in Eqs. (5) and (7), Eq. (18) is expressed as

$$\sum_{j=1}^{N} q^{(j)^T} \cdot u + \varepsilon_o \sum_{j=1}^{N} \left(\lambda^{(j)} - q^{(j)^T} u_\varepsilon^{(j)} \right)$$
$$= \rho \omega^2 \sum_{j=1}^{N} \left(q^{(j)^T} u_\omega^{(j)} - \mu^{(j)} \right) + \Delta T \sum_{j=1}^{N} \left(q^{(j)^T} u_T^{(j)} - \chi^{(j)} \right) \qquad (19)$$

In Eq. (19), j denotes a ring number and q of a j-th ring is defined as follows (the superscript j is omitted for clarity):

$$q = g^T \Phi^{-1} G^{-1} \qquad (20)$$

where

$$g = \begin{bmatrix} \alpha \varphi_1 \left(r_o^{\kappa+1} - r_i^{\kappa+1} \right) \\ \beta \varphi_2 \left(r_o^{-\kappa+1} - r_i^{-\kappa+1} \right) \end{bmatrix} \qquad (21)$$

In Eq. (19) and Eq. (21), the following symbols are defined:

$$\lambda = \left[(Q_{21} + Q_{23}) \varphi_3 + Q_{22} \right] \frac{(r_o^2 - r_i^2)}{2}, \quad \mu = -(Q_{21} + 3Q_{23}) \varphi_0 \frac{(r_o^4 - r_i^4)}{4},$$

$$\alpha = \left[\frac{Q_{21} - Q_{23}}{\kappa + 1} + Q_{23} \right], \quad \beta = \left[\frac{Q_{21} - Q_{23}}{(-\kappa + 1)} + Q_{23} \right] \qquad (22)$$

$$\text{and } \chi = \left[(Q_{21} + Q_{23}) \varphi_{T1} - \beta_z \right] \frac{(r_o^2 - r_i^2)}{2}$$

Eqs. (1)-(19) apply to any arbitrary ring. At each interface between two adjacent rings (e.g., j and $j+1$), the continuous radial traction and continuous radial displacement should be satisfied as illustrated in Figure 2:

$$\sigma_{r_i}^{(j+1)} = \sigma_{r_o}^{(j)} \quad \text{and} \quad u_{r_i}^{(j+1)} = u_{r_o}^{(j)} \qquad (23)$$

Combining all the ring stiffness matrix in Eq. (14) by using the continuity equations yields the global stiffness matrix equation

9

$$\begin{bmatrix} K_{uu} & K_{u\varepsilon} \\ K_{\varepsilon u} & K_{\varepsilon\varepsilon} \end{bmatrix} \begin{bmatrix} U \\ \varepsilon_o \end{bmatrix} = \begin{bmatrix} F_b \\ 0 \end{bmatrix} + \rho\omega^2 \begin{bmatrix} F_\omega \\ F'_\omega \end{bmatrix} + \Delta T \begin{bmatrix} F_T \\ F'_T \end{bmatrix} \qquad (24)$$

where

$$K_{uu} = \sum_{j=1}^{N} k^{(j)}, \quad K_{u\varepsilon} - K_{\varepsilon u} - \sum_{j=1}^{N} q^{(j)^T} \quad \text{and} \quad K_{\varepsilon\varepsilon} - \sum_{j=1}^{N} \left(\lambda^{(j)} - q^{(j)^T} u_\varepsilon^{(j)} \right) \qquad (25)$$

The global displacement vector U consists of $N+1$ displacements at all the radii of the rings. The global force vectors $F_b, F_\omega, F'_\omega, F_T$ and F'_T in Eq. (24) are as follows;

$$F_b - \sum_{j=1}^{N} f_b^{(j)} - \left(-r_1 \sigma_{r_i}^{(1)} \quad 0 \quad \cdots \quad 0 \quad r_{N+1} \sigma_{r_o}^{(N)} \right)^T$$

$$F_\omega = \sum_{j=1}^{N} f_\omega^{(j)}, \quad F'_\omega - \sum_{j=1}^{N} \left(q^{(j)^T} u_\omega^{(j)} - \mu^{(j)} \right) \qquad (26)$$

$$F_T = \sum_{j=1}^{N} f_T^{(j)} \quad \text{and} \quad F'_T - \sum_{j=1}^{N} \left(q^{(j)^T} u_T^{(j)} - \chi^{(j)} \right)$$

Notice that the global stiffness matrix is symmetric, and F_b has only the boundary pressures given at the inner and outer surfaces since the internal stresses were canceled out due to the stress continuity condition. F_ω is an internal inertial force vector due to the rotation.

Now we can solve the system of $N+2$ equations and obtain the radial displacements $u^{(j)}$ at each interface and constant axial strain ε_o. The strains in cylindrical coordinates are then calculated using the relationship in Eq. (4).

3.2 Strength Analysis

The on-axis strains $\bar{\varepsilon}$ in the material symmetric axes are obtained by transforming the off-axis strains ε in the cylindrical coordinates[25] as shown in Figure 2:

$$\bar{\varepsilon} = T\varepsilon \qquad (27)$$

where T is a transformation matrix defined in terms of a ply angle ϕ;

$$T = \begin{bmatrix} \cos^2\phi & \sin^2\phi & 0 & \cos\phi\sin\phi \\ \sin^2\phi & \cos^2\phi & 0 & -\cos\phi\sin\phi \\ 0 & 0 & 1 & 0 \\ 2\cos\phi\sin\phi & 2\cos\phi\sin\phi & 0 & \cos^2\phi \quad \sin^2\phi \end{bmatrix} \qquad (28)$$

10

The on-axis stress $\bar{\sigma}$ is then calculated using the stress-strain relationship:

$$\bar{\sigma} = \bar{Q}(\bar{\varepsilon} - \bar{\alpha}\Delta T) \tag{29}$$

The on-axis stiffness matrix $\bar{Q}$ and the coefficients of thermal expansion (CTE) $\bar{\alpha}$ in Eq. (29) are given by the material properties[25]:

$$\bar{Q} = \begin{bmatrix} 1/E_{\bar{\theta}} & -\nu_{\bar{\theta}\bar{r}}/E_{\bar{r}} & -\nu_{\bar{\theta}\bar{z}}/E_{\bar{z}} & 0 \\ & 1/E_{\bar{r}} & -\nu_{\bar{r}\bar{z}}/E_{\bar{z}} & 0 \\ & & 1/E_{\bar{z}} & 0 \\ sym. & & & 1/G_{\bar{\theta}\bar{z}} \end{bmatrix}^{-1} \quad \text{and} \quad \bar{\alpha} = \begin{pmatrix} \alpha_{\bar{\theta}} \\ \alpha_{\bar{r}} \\ \alpha_{\bar{z}} \\ 0 \end{pmatrix} \tag{30}$$

The definitions of Moduli, Poisson's Ratios, and CTE in Eq. (30) are explained in Table 1.

Once the on-axis stresses in the j-th ring are calculated, a failure of the material can be accessed by using a failure criterion. In this study, 3-dimensional Tsai-Wu quadratic failure criterion[19] is used:

$$\bar{\sigma}^T \tilde{F} \bar{\sigma} + \bar{F}\bar{\sigma}R - R^2 = 0 \tag{31}$$

Solving Eq. (31) yields a strength ratio R indicating material failure with a value greater than 1. When the strength ratio $R < 1$, the applied stresses can increase by a factor of its inverse before material failure occurs. The strength parameters $\tilde{F}$ and $\bar{F}$ are defined in terms of the material strengths:

$$\tilde{F} = \begin{bmatrix} \dfrac{1}{XX'} & -\dfrac{1}{2}\sqrt{\dfrac{1}{XX'}\dfrac{1}{YY'}} & -\dfrac{1}{2}\sqrt{\dfrac{1}{XX'}\dfrac{1}{YY'}} & 0 \\ -\dfrac{1}{2}\sqrt{\dfrac{1}{XX'}\dfrac{1}{YY'}} & \dfrac{1}{YY'} & -\dfrac{1}{2YY'} & 0 \\ -\dfrac{1}{2}\sqrt{\dfrac{1}{XX'}\dfrac{1}{YY'}} & -\dfrac{1}{2YY'} & \dfrac{1}{YY'} & 0 \\ 0 & 0 & 0 & \dfrac{1}{S^2} \end{bmatrix} \tag{32}$$

$$\bar{F} = \begin{bmatrix} \dfrac{1}{X} - \dfrac{1}{X'} & \dfrac{1}{Y} - \dfrac{1}{Y'} & \dfrac{1}{Y} - \dfrac{1}{Y'} & 0 \end{bmatrix} \tag{33}$$

where X and X' are the tensile and compressive strengths in the fiber direction, Y and Y' those in the matrix direction, and S the shear strength.
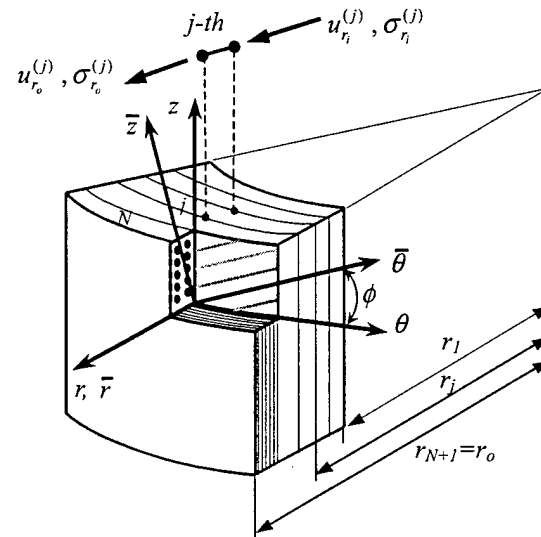
Figure 1. Model of multi-ringed composite flywheel rotor with the angle ply $[(+/-\phi)_m]$ in each rings. The radial displacement and stress of j-th element components, and the off-axis coordinate (θ, z, r) and the on-axis coordinate $(\bar{\theta}, \bar{z}, \bar{r})$ systems are defined.

4. COMPARISION OF 2-D & 3-D SOLUTIONS

Three types of two-dimensional analyses based on the assumptions in the axial deformation and stresses, i.e., plane stress (PSS), plane strain (PSN), and generalized plane strain (GPS) are described in the previous chapter. The accuracy of the two-dimensional analyses of the flywheel rotor with the residual stresses depend upon the length and material properties of the rotor and the boundary condition at the axial ends of the rotor. However, either one of them cannot perfectly match with three-dimensional analysis. In this chapter, the two-dimensional analyses will be compared with the three-dimensional analysis using the commercial finite element analysis program ANSYS. The full three-dimensional solutions with a consideration of the rotor length, the material hybridization, and the helical winding are obtained and compared with three different two-dimensional solutions, i.e., PSS, PSN, and GPS. The symmetry of the rotor enables to analyze the one-eighth portion of the rotor in the three-dimensional finite element analysis of the rotor as shown in Figure 2. Eight-node hexagonal element with each node having three degree-of-freedoms is used for the analysis.

Total of 6 cases are considered, all with the same ID as 75 mm and OD as 221 mm. First 3 cases are for the hybrid rotor of Glass/Epoxy and T300/5208, and the rest 3 cases are for the helically wound rotor of T300/5208. The specifications of the cases are summarized and listed in Table 1. Their material properties are shown in Table 2. The case 1 is a reference case to compare with other cases of hybrid rotors. In case 2, the length is changed; in case 3, the rotational forces are applied instead of the thermal loading. In case 4, the winding with the angle of 45 degrees for the half of the total radial thickness and then hoop winding for the rest of half are considered. In case 5, the length is changed, and in case 6 the helical winding angles are linearly changed from 45 degrees at the inner surface to 0 degree at the outer surface.

The radial, hoop, and axial stresses and strains for the 6 cases are calculated by both three-dimensional finite element and the two-dimensional methods, and they are shown in Figures 3~8. In the three-dimensional analyses, the solutions are obtained at the middle and top surfaces of the rotor. The stresses and strains at the top surface in the longer rotor slightly but negligibly differ from those of shorter rotor, as shown Figures 3 and 4. The

13

PSS and GPS solutions match well with the 3-D solutions at the middle surface, which can be considered to be representative of the rotor status since they show a little higher values than at the top surface. On the other hand, the PSN solution is far higher than other solutions. Notice that the axial stains can be well predicted using the PSS solution. In the case 3, both GPS and PSS solutions also well predict the 3-D solution. The axial strain in case 3 can be best predicted by the PSS. In cases 4 and 5, the stresses at the top are quite higher than those at the middle. We can notice that the abrupt change of winding angles from 45 to 0 degree causes the high radial stress variation around the interface, which cannot be well predicted by any of 2-dimensional analyses. The radial stress variation around the interface at the top surface is higher in the case 5 in which the rotor is longer than the case 4. However, except the region near the top surface the GPS solution is closer to the 3-D solution. In the case 6 where the winding angles are linearly changing along the radius, the 3-D solutions at both top and middle surfaces coincide with each other and can be best predicted by the PSS solution.

As a conclusion, both PSS and GPS solutions yield the better solution than PSN in all cases. Since the implementation of GPS analysis into a computer code takes more efforts than the PSS, the PSS solution is the best in prediction the stresses and strains of the flywheel rotor, regardless of the hybridization and helical winding, and the thermal and rotational forces. However, care should be taken in applying the 2-D analysis to the rotor with abrupt changes of fiber winding angles.

14
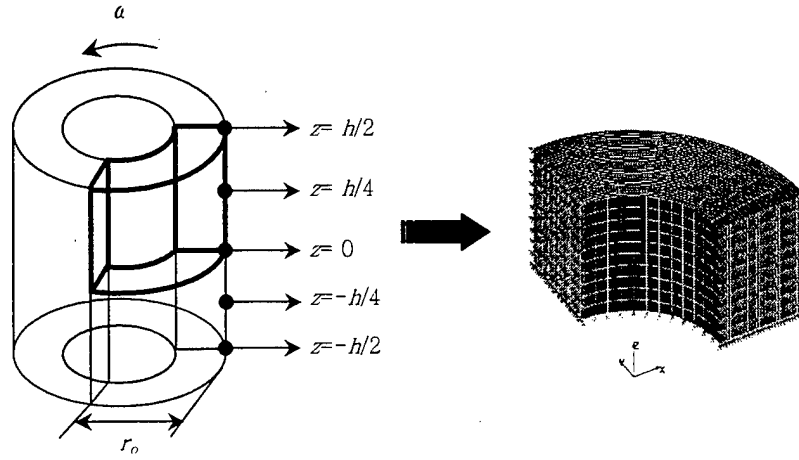
Figure 2. One eighth of composite flywheel rotor for 3-D finite element analysis.

Table 1. Specifications of the cases

	Hybrid Rotor			Helical Rotor		
Case	1	2	3	4	5	6
ID (mm)	75	75	75	75	75	75
Thickness (mm)	36.5/36.5	36.5/36.5	36.5/36.5	36.5/36.5	36.5/36.5	73.0
Height (mm)	35	220	35	35	220	35
Materials	E-glass/Epoxy T300/5208	E-glass/Epoxy T300/5208	E-glass/Epoxy T300/5208	T300/5208	T300/5208	T300/5208
Angles (°)	0 / 0	0 / 0	0 / 0	45 / 0	45 / 0	45 /.../ 0
ΔT (°C)	-100	-100	•	-100	-100	-100
RPM	•	•	10,000	•	•	•

Table 2. Material properties

Material data	T300/5208	E-glass/Epoxy ($v_f = 0.45$)	E-glass/Epoxy ($v_f = 0.65$)
E_x (GPa)	181	38.6	56.96
$E_y = E_z$ (GPa)	10.3	8.27	8.27
$\nu_{xy} = \nu_{xz}$	0.28	0.26	0.26
ν_{yz}	0.3	0.3	0.3
$G_{xy} = G_{xz}$ (GPa)	7.17	4.14	7.16
G_{yz} (GPa)	3.4	3.4	3.4
α_x (μm/m)/K	2.0 E-6	8.6 E-6	6.12 E-6
$\alpha_y = \alpha_z$ (μm/m)/K	22.5 E-6	2.1 E-6	16.2 E-6
ρ (kg /m^3)	1600	1800	2066

15
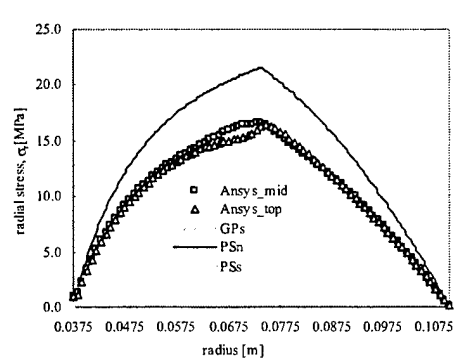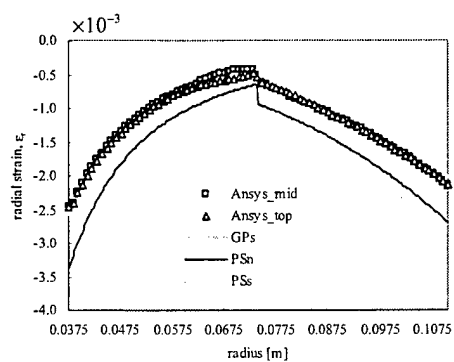
(a) radial stresses

(d) radial strains

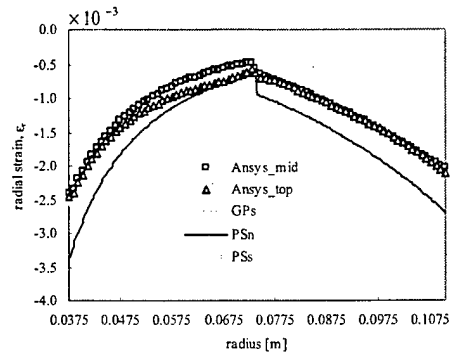(b) hoop stresses
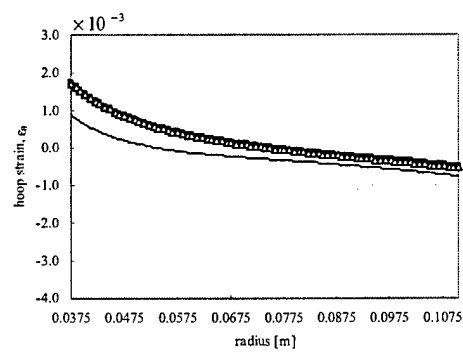
(e) hoop strains
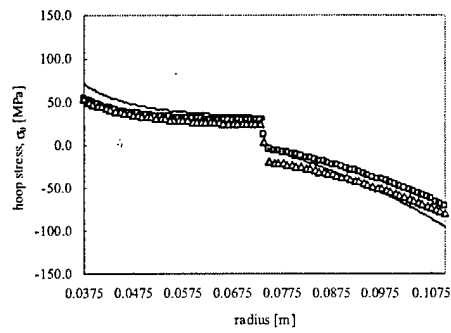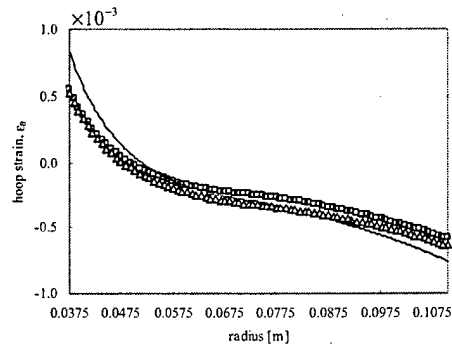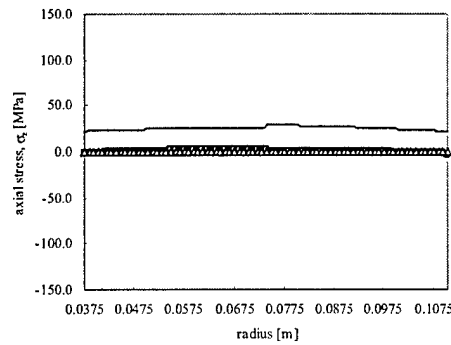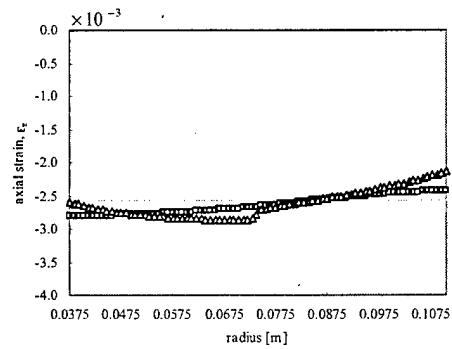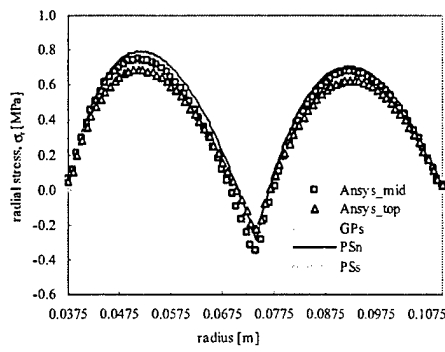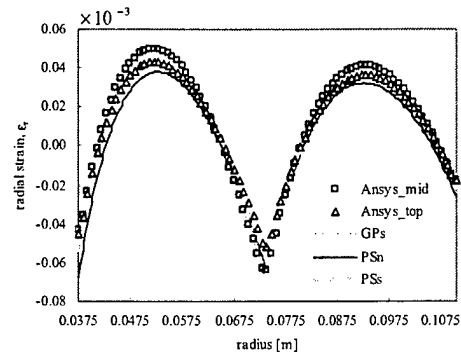
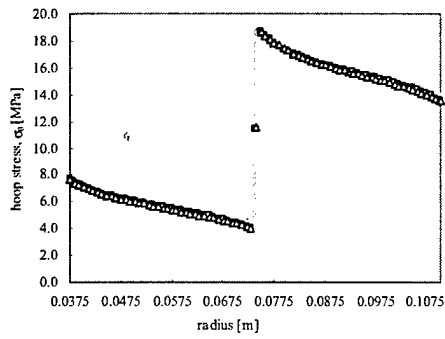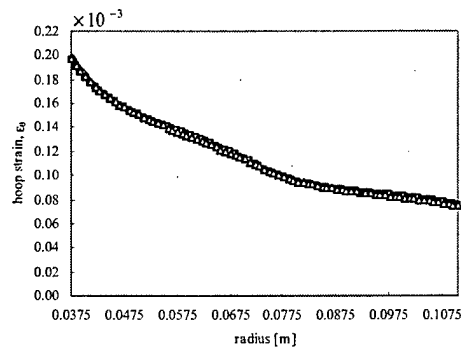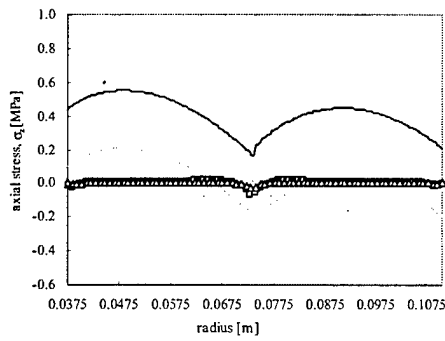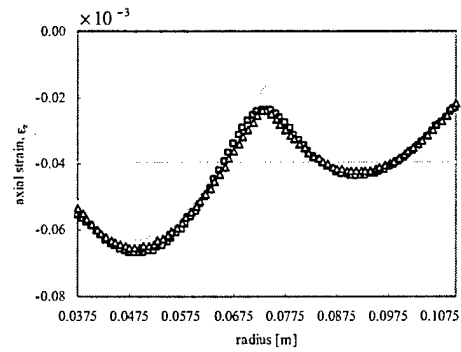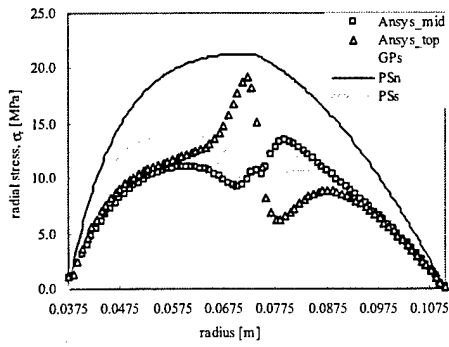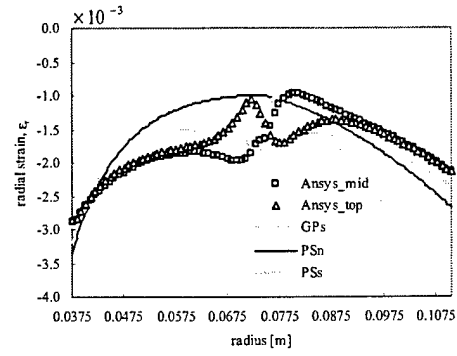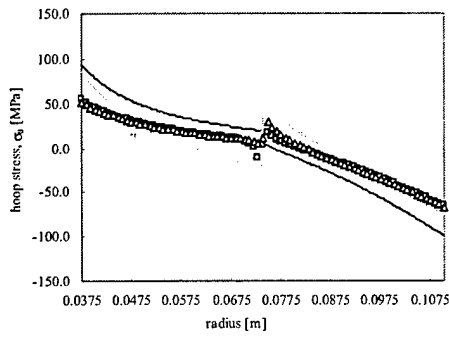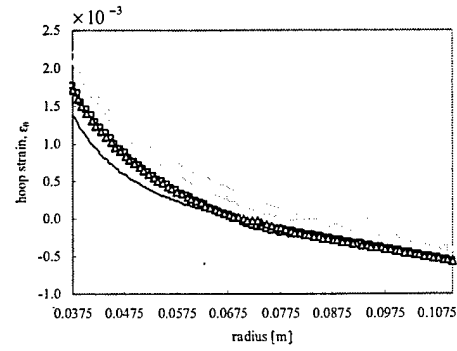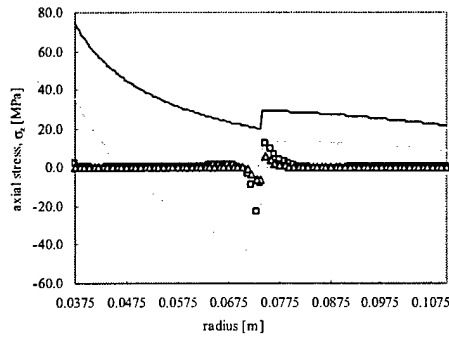(c) axial stresses

(f) axial strains

Figure 3. Distribution of radial, hoop, and axial stresses and stains of case 1

16

25.0

20.0

15.0

radial stress, σ_r [MPa]

10.0

5.0

0.0

Ansys_mid

Ansys_top

GPs

PSn

PSs

0.0375 0.0475 0.0575 0.0675 0.0775 0.0875 0.0975 0.1075

radius [m]

(a) radial stresses

$\times 10^{-3}$

0.0

-0.5

-1.0

radial strain, ε_r

-1.5

-2.0

-2.5

-3.0

-3.5

-4.0

Ansys_mid

Ansys_top

GPs

PSn

PSs

0.0375 0.0475 0.0575 0.0675 0.0775 0.0875 0.0975 0.1075

radius [m]

(d) radial strains

150.0

100.0

50.0

hoop stress, σ_θ [MPa]

0.0

-50.0

-100.0

-150.0

0.0375 0.0475 0.0575 0.0675 0.0775 0.0875 0.0975 0.1075

radius [m]

(b) hoop stresses

$\times 10^{-3}$

1.0

0.5

hoop strain, ε_θ

0.0

-0.5

-1.0

0.0375 0.0475 0.0575 0.0675 0.0775 0.0875 0.0975 0.1075

radius [m]

(e) hoop strains

150.0

100.0

50.0

axial stress, σ_z [MPa]

0.0

-50.0

-100.0

-150.0

0.0375 0.0475 0.0575 0.0675 0.0775 0.0875 0.0975 0.1075

radius [m]

(c) axial stresses

$\times 10^{-3}$

0.0

-0.5

-1.0

axial strain, ε_z

-1.5

-2.0

-2.5

-3.0

-3.5

-4.0

0.0375 0.0475 0.0575 0.0675 0.0775 0.0875 0.0975 0.1075

radius [m]

(f) axial strains

Figure 4. Distribution of radial, hoop, and axial stresses and stains of case 2

17

(a) radial stresses

(b) hoop stresses

(c) axial stresses

(d) radial strains

(e) hoop strains

(f) axial strains

Figure 5. Distribution of radial, hoop, and axial stresses and stains of case 3

(a) radial stresses

(b) hoop stresses

(c) axial stresses

(d) radial strains

(e) hoop strains

(f) axial strains

Figure 6. Distribution of radial, hoop, and axial stresses and stains of case 4

19

(a) radial stresses

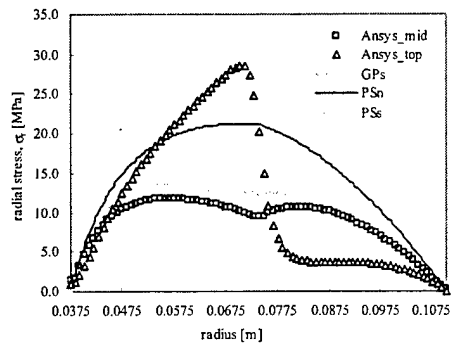(b) hoop stresses

(c) axial stresses

(d) radial strains

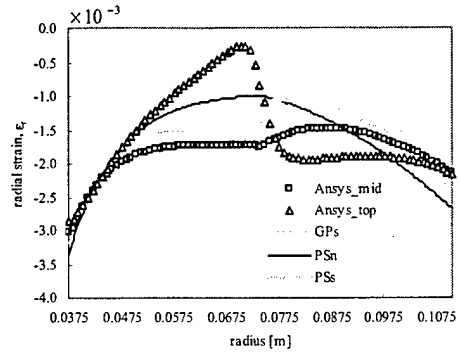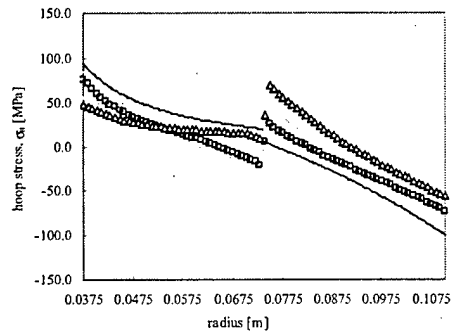(e) hoop strains

(f) axial strains

Figure 7. Distribution of radial, hoop, and axial stresses and stains of case 5

20

(a) radial stresses

(b) hoop stresses
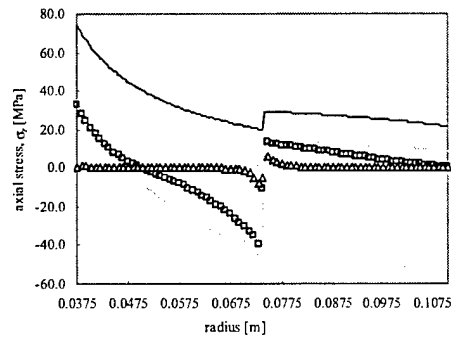
(c) axial stresses
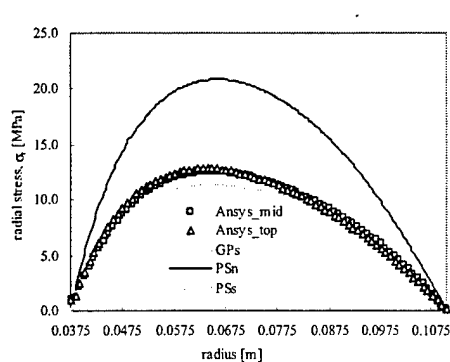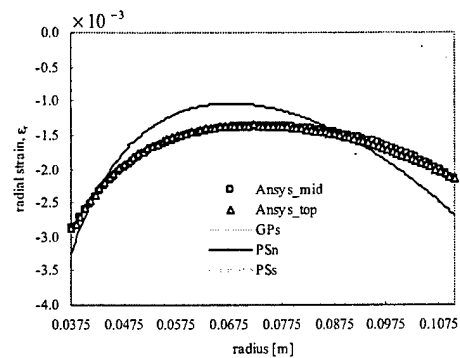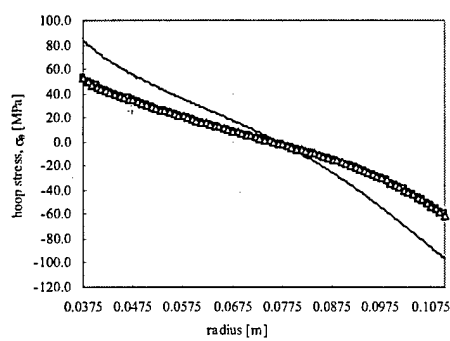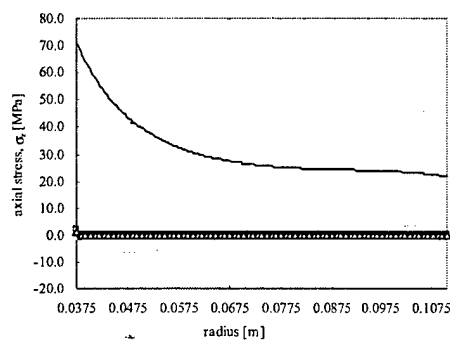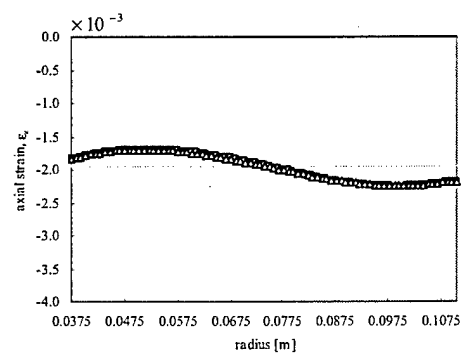
(d) radial strains

(e) hoop strains

(f) axial strains

Figure 8. Distribution of radial, hoop, and axial stresses and stains of case 6

21

5. PROCESS INDUCED RESIDUAL STRESSES

The flywheel rotor of composite materials has characteristics of distinctively high energy density, long life and lightweight. An advanced composite flywheel has thus attracted the considerable attentions of many investigators for various energy storage applications such as electric utilities, hybrid or electric vehicles and spacecraft [1-5]. Recent efforts in development of the flywheel have been devoted to the experimental and theoretical investigation on increasing the performance, while insuring the safety of the flywheel, along with technical innovations in high stiffness and strength composite materials.

In the design of such high performance flywheel rotor, how to hybridize the composite materials, i.e., determination of the material sequence and the thickness, is crucial in minimizing the radial stresses caused by the high rotating speed [6]. The influences of the centrifugal forces on the mechanical behavior of the rotor have thus been successfully analyzed in design of a thick wound composite rotor [7-10]. However, as the thickness of the rotor increases, manufacturing process of the thick section polymer composite rotors can generate the residual stresses which add to those generated by the centrifugal forces and significantly deteriorate the performance of the flywheel rotor [10,11].

Wet winding, followed by the stages of heat buildup, curing, and cooling, is a typical process for manufacturing the thick composite rotor. During heat buildup, the radial stiffness decrease and the stresses are relaxed, and upon curing the radial stiffness and transverse strength increase and simultaneous chemical shrinkage occurs. Cooling is associated with simultaneous thermal shrinkage of both the rotor and the mandrel [12-16]. Especially, the cool-down stage in the curing process cause the tremendous amount of radial tensile stresses primarily due to the anisotropic thermal expansion of individual plies. During the entire history of the manufacturing process, the mechanical properties and stress-strain state may undergo a significant change.

Several investigators have developed theoretical models of the whole filament winding process [13-17]. Among several attempts, Lee et al. modeled the processes applicable to the moderately thick cylinders [14-16] by establishing submodels, each for

thermochemical behavior, fiber motion, void, and stress, and developed a cure simulation computer program called WINDTHICK [16]. Even though the models are well established, we should supply many parameters for the material properties to simulate the program. Among them the material properties of the uncured composite fiber and resin and their variation along with the temperature and the degree of cure are rarely handy. Therefore, the complexities involved in these models makes it difficult to be used as a design tool, especially for the optimization of the composite cylinder.

For a design tool for the thick wound cylinder, a relatively simplified model was proposed which mainly consider the thermal expansion and detachment of the mandrel and the cooldown of the cylinder [11]. In the work it is found that main factors influencing the stress state for some helically wound composite cylinders are the temperature change and the chemical shrinkage, and not the fiber tension nor motion. In that model, however, the detachment between the mandrel and the cylinder should be still modeled, and the material properties of the uncured composites need to be given. It is observed in other work that the thickness and the material properties of the mandrel can affect the residual stresses in the composite cylinder [19]. However, those stresses vary according to the thickness ratio of the mandrel and the composite cylinder.

It has been observed that the curing process for moderately thick (e.g. 2" thickness for 4" ID) graphite wound composite cylinder can even cause a radial delamination [11]. However, the experimental measurement of the residual stresses and strains of the thick wound rotor has been rarely performed in comparison to the relatively thin rotors [18-20]. Moreover, the detection of the delamination present in the thick wound cylinders never been reported.

Compared to the conventional one-stage cure, the residual stress advantages can be realized by the multi-staged curing method, where layers of materials are allowed to harden for a time period before more materials are wound onto the rotor. An in-situ curing can be a more productive way than the staged curing method, and a simplified analysis of residual stresses related to this process has been investigated by Bakis et al. [21]. Nevertheless, the one-stage cure is always a more productive method as long as the residual stresses are properly managed.

In this study, in order to estimate the stresses and strains accumulated inside the

23

rotor during the manufacturing process of the thick wound cylinder, a simplified theoretical analysis using the material properties only at room temperature and the equivalent thermal loading is presented. The validity of the method is examined by comparison with the results from the cure simulation program WINDTHICK. The experimental test was also performed where the residual stresses were released by splitting the rotor in the radial direction, while measuring the strains [22,23]. Most importantly, the residual stresses and strains that are high enough to cause the radial delamination have been studied and experimentally measured.

5.1 Stress and Strength Analysis of a Hoop Wound Cylinder

A stress analysis of a hoop wound composite cylinder is performed with a consideration of the process induced residual strains that mainly result from the temperature drop and the chemical shrinkage. A linear plane stress-strain relationship considering the thermal strains and chemical shrinkage in a cylindrical coordinate system can be written as

$$\begin{pmatrix} \sigma_\theta \\ \sigma_r \end{pmatrix} = \begin{bmatrix} Q_{11} & Q_{12} \\ Q_{21} & Q_{22} \end{bmatrix} \left\{ \begin{pmatrix} \varepsilon_\theta \\ \varepsilon_r \end{pmatrix} - \begin{pmatrix} \alpha_\theta \\ \alpha_r \end{pmatrix} \Delta T_c - \begin{pmatrix} \varepsilon_\theta \\ \varepsilon_r \end{pmatrix}_{sh} \right\} \tag{34}$$

where σ_r, σ_θ, ε_r and ε_θ are the radial and hoop stresses and strains, respectively. The coefficients of thermal expansion (CTE) are denoted by α_θ and α_r. A typical temperature change ΔT_c in the curing process is considered as the difference between the maximum cure temperature and the room temperature. In general, the chemical shrinkage occurring in the process can be hardly measured. However, since both thermal strains and chemical shrinkages of the composite materials mainly result from the deformation of the matrix, each magnitude of the chemical shrinkage in the hoop and radial directions is assumed to have the same ratio as the thermal strains. Hence, Eq. (34) can be written as

$$\begin{pmatrix} \sigma_\theta \\ \sigma_r \end{pmatrix} = \begin{bmatrix} Q_{11} & Q_{12} \\ Q_{21} & Q_{22} \end{bmatrix} \left\{ \begin{pmatrix} \varepsilon_\theta \\ \varepsilon_r \end{pmatrix} - \begin{pmatrix} \alpha_\theta \\ \alpha_r \end{pmatrix} \Delta T \right\} \tag{35}$$

where an effective temperature change $\Delta \bar{T}$ contains both ΔT_c and a temperature drop

24

ΔT_{sh} equivalent to the chemical shrinkage:

$$\Delta \tilde{T} = \Delta T_c + \Delta T_{sh} \qquad (36)$$

To derive the stresses and strains due to the effective temperature change $\Delta \tilde{T}$, Eq.(35) is rewritten as

$$\begin{pmatrix} \sigma_\theta \\ \sigma_r \end{pmatrix} = \begin{bmatrix} Q_{11} & Q_{12} \\ Q_{21} & Q_{22} \end{bmatrix} \begin{pmatrix} \varepsilon_\theta \\ \varepsilon_r \end{pmatrix} - \begin{pmatrix} \beta_\theta \\ \beta_r \end{pmatrix} \Delta T \qquad (37)$$

where $\beta = Qa$.

The stress distribution of a hoop wound composite cylinder is governed by the radial equilibrium equation, which is written in cylindrical coordinates as [24~26]

$$\frac{d\sigma_r}{dr} + \frac{\sigma_r - \sigma_\theta}{r} = 0 \qquad (38)$$

The circumferential and radial strains are expressed by the r-direction displacement u_r:

$$\varepsilon_\theta = \frac{u_r}{r}, \varepsilon_r = \frac{\partial u_r}{\partial r} \qquad (39)$$

Substituting Eqs. (37) and (39) into Eq. (38) yields the radial and hoop stresses and strains:

$$\sigma_r = C_1 \varphi_1 \bar{r}^{\kappa-1} + C_2 \varphi_2 \bar{r}^{-\kappa-1} + \varphi_{T2} \Delta \tilde{T} \qquad (40a)$$

$$\varepsilon_r = \kappa C_1 \varphi_1 \bar{r}^{\kappa-1} + \kappa C_2 \varphi_2 \bar{r}^{-\kappa-1} + \varphi_{T1} \Delta \tilde{T} \qquad (40b)$$

$$\sigma_\theta = \kappa C_1 \bar{r}^{\kappa-1} - \kappa C_2 \bar{r}^{-\kappa-1} + \varphi_{T2} \Delta \tilde{T} \qquad (41a)$$

$$\varepsilon_\theta = C_1 \varphi_1 \bar{r}^{\kappa-1} - C_2 \varphi_2 \bar{r}^{-\kappa-1} + \varphi_{T1} \Delta \tilde{T} \qquad (41b)$$

where the radial coordinate is normalized by the inner radius r_i, denoted by $\bar{r}$. The symbols κ and φ_i are defined in terms of the material properties:

$$\kappa = \sqrt{\frac{Q_{11}}{Q_{22}}}, \quad \varphi_1 = \frac{1}{\kappa Q_{22} + Q_{12}}, \quad \varphi_2 = \frac{1}{\kappa Q_{22} - Q_{12}}, \qquad (42a)$$

$$\varphi_{T1} = \frac{\beta_\theta - \beta_r}{Q_{11} - Q_{22}}, \text{ and } \varphi_{T2} = (Q_{12} + Q_{22})\varphi_{T1} - \beta_r \qquad (42b)$$

Unknown constants C_1 and C_2 are determined from the boundary conditions, i.e. $\sigma_r=0$ at $r=r_i$ and $r=r_o$:

$$C_1 = \frac{1 - \bar{r}_o^{-\kappa-1}}{\bar{r}_o^{-\kappa-1} - \bar{r}_o^{\kappa-1}}\varphi_{T2}\Delta\tilde{T}, \quad C_2 = \frac{\bar{r}_o^{\kappa-1} - 1}{\bar{r}_o^{-\kappa-1} - \bar{r}_o^{\kappa-1}}\varphi_{T2}\Delta\tilde{T} \tag{43}$$

where $\bar{r}_o$ is the dimensionless outer radius normalized by the inner radius.

The radial delamination can occurs within the cylinder due to the residual stresses. In the absence of the shear stress, two simple delamination criterions can be used, i.e., a maximum stress criterion and a maximum strain criterion [25]:

$$\frac{\sigma_r}{Y} = D_\sigma \tag{44a}$$

$$\frac{\varepsilon_r}{Y/E_r} = D_\varepsilon \tag{44b}$$

Delamination occurs when the delamination index D_σ or D_ε reaches the value of one. Once a delamination occurs, it is assumed that the cylinder is split into two cylinders. The radial location where the maximum delamination index occurs is derived from the condition that $\partial D/\partial r = 0$ in Eq. (44), each yielding

$$\bar{r}_{max\_\sigma} = \left(\frac{\bar{r}_o^{\kappa-1} - 1}{1 - \bar{r}_o^{-\kappa-1}}\frac{\kappa+1}{\kappa-1} \right)^{\frac{1}{2\kappa}} \tag{45a}$$

$$\bar{r}_{max\_\varepsilon} = \left(\frac{\varphi_2}{\varphi_1} \right)^{\frac{1}{2\kappa}} \bar{r}_{max\_\sigma} \tag{45b}$$

It is noted that the radial location $\bar{r}_{max\_\sigma}$, where the maximum index D_σ, or the maximum radial stress occurs, is a function of only $\bar{r}_o$ and κ, independent of the CTE α_ϑ and α_r. And $\bar{r}_{max\_\varepsilon}$ is always located farther than $\bar{r}_{max\_\sigma}$ from the center of the cylinder. Substitution of Eq.(45a) into Eq.(40a) then yields the maximum radial stress; Eq.(45b) into Eq.(40b) yields the maximum radial strain. Using these formulae together with either Eq.(44a) or (44b), the maximum temperature drops which cause delamination are obtained, each denoted by $\Delta\tilde{T}_{d\_\sigma}$ and $\Delta\tilde{T}_{d\_\varepsilon}$:

$$\Delta\tilde{T}_{d\_\sigma} = \frac{1}{\varphi_{T2}}\frac{(\bar{r}_o^{-\kappa-1} - \bar{r}_o^{\kappa-1})Y}{(1 - \bar{r}_o^{-\kappa-1})\bar{r}_{max\_\sigma}^{\kappa-1} + (\bar{r}_o^{\kappa-1} - 1)\bar{r}_{max\_\sigma}^{-\kappa-1} + 1} \tag{46a}$$

26

$$\Delta \tilde{T}_{d\_\varepsilon} = \frac{1}{\varphi_{T2}} \frac{(\bar{r}_o^{-\kappa-1} - \bar{r}_o^{\kappa-1})Y / E_r}{(1 - \bar{r}_o^{-\kappa-1})\bar{r}_{\max\_\varepsilon}^{\kappa-1}\kappa\varphi_1 + (\bar{r}_o^{\kappa-1} - 1)\bar{r}_{\max\_\varepsilon}^{-\kappa-1}\kappa\varphi_2 + \varphi_{T1} / \varphi_{T2}} \qquad (46b)$$

It is noted that both $\Delta \tilde{T}_{d\_\sigma}$ and $\Delta \tilde{T}_{d\_\varepsilon}$ are functions of the dimensionless radius $\bar{r}_o = r_o / r_i$. In other words, the cylinders of the geometric similarity experience a delamination at the same temperature drop. It can be thus deduced that the larger cylinder is more advantageous in decreasing the thermal stresses, especially in the flywheel rotor.

5.2 Cure Simulation by WINDTHICK

The cure-simulation program WINDTHICK is used to determine the major factors affecting the residual stresses within the thick wound composite cylinder among the process parameters or models, which include (1) fiber winding tension and motion, (2) thermochemical evolution, (3) interaction with the mandrel, and (4) change of composite material properties with respect to the temperature and the degree of cure. The simple stress analysis presented in the previous chapter is then performed using only the material properties of the cured composites rather than considering in detail the variation of the material properties along with the degree of cure. It is then shown that the total residual stresses can be well represented by the effective temperature drop.

To validate the approach, residual stresses are calculated for thick cylinders in two cases which was considered by Lee et at. [16]. Fiberite T300/976 is used, and the material properties and cure cycles are summarized in [16]. Composite cylinders are wound on a 4 inch diameter, 0.25 inch thick aluminum mandrel. Two stacking sequences are considered, i.e., $[-55/+55]_{50}$ and $[(\pm 45)_{15}, 90_{40}, (\pm 45)_{15}]$. Each cylinder consists of 100 layers, and the corresponding wall thickness is 2 inches. Room temperature and maximum cure temperature are taken respectively as 65 °F and 350 °F [16]. The calculation is performed in two ways; one with the full model considered by Lee et al. [16] and the other with the simple model in which the cured material properties are used together with the temperature drop and the chemical shrinkage. In the simple model, the temperature drop for both cases is given as the difference between the room and maximum cure temperatures, i.e. T_c= 65 °F -350 °F = -285 °F, and the chemical shrinkage as ε_{sh}=0.5%.

27

The calculated radial and hoop stresses are in good agreement with the results by the program WINDTHICK within 3% of error.

As a second case, the effects of the rotor thickness on the residual stresses are investigated. Three cylinders A, B and C of different outer radii, i.e. 77, 110.5, and 152.5 mm are considered with the same 37.5 mm inner diameters, and they are all hoop wound. The cure cycle is chosen to fully cure the cylinders. All other parameters such as the mechanical properties of the mandrel and the composites are the same as the first case. The radial and hoop stresses are calculated and shown in Figure 9. It is once again shown that the results by the simple stress analysis are very close to those by the full model. It is noticed that the same temperature drop of T_c= -285 °F and chemical shrinkage of 0.5 % for all three cylinders in the simple model can represent the residual stresses from the full model.

It is concluded in this section that the temperature drop and the chemical shrinkage are the major sources for the residual stresses within the thick wound composite cylinder, not the interaction with the mandrel nor the fiber tension and motion. In other words, the distribution of the process-induced residual stresses can be obtained, regardless of the rotor thickness, from the cured composite cylinder experiencing a uniform temperature drop and chemical shrinkage throughout the rotor. The results by the simple stress analysis can be also obtainable from the WINDTHICK program with the exclusion of the thermal expansion of the mandrel, the fiber tension and motion and the dependency of the material properties upon the degree of cure.
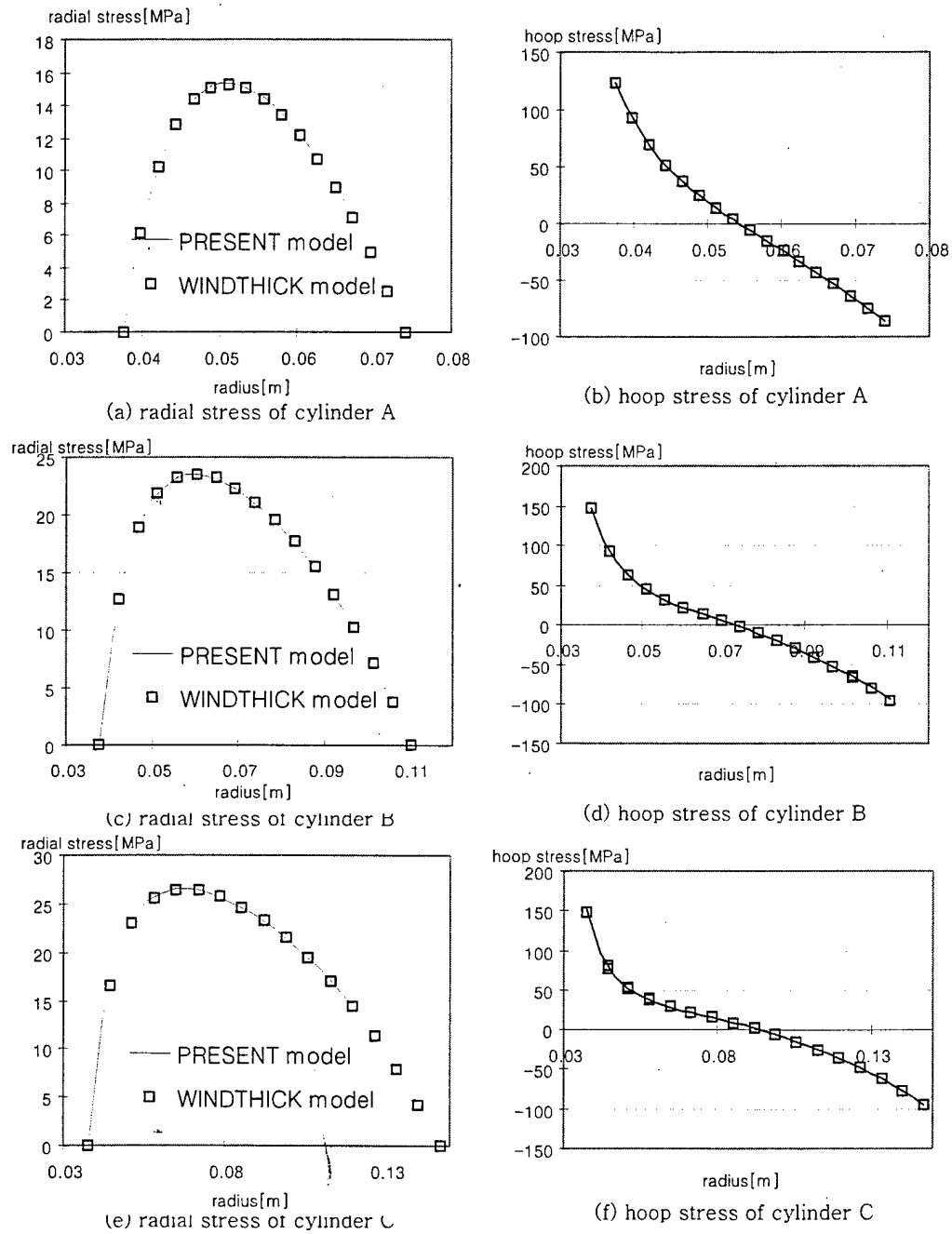
(a) radial stress of cylinder A

(b) hoop stress of cylinder A

(c) radial stress of cylinder B

(d) hoop stress of cylinder B

(e) radial stress of cylinder C

(f) hoop stress of cylinder C

Figure 9. Residual stresses within three cylinders of three different sizes.

29

5.3 Split Ring Test Method

The residual strains are measured using a split ring method. The strain gages are glued to the side surfaces of the cured cylinder. The cylinder is then split by cutting along the radial direction, and the residual stresses are released. The stress-released strains are measured.

Assuming that the stresses and strains are zero through out the rotor just before cooling down from the cure temperature, the residual strains and stresses have been accumulated during the effective temperature drop $\Delta \tilde{T}$. Theses residual stress and strain state can be viewed as a sum of two consecutive states; stress-free temperature drop followed by application of the mechanical stresses to the radial surfaces. The typical stress and strain distribution and a superposition procedure are illustrated in Figure 10. The stains of the stress-free specimen due to the pure temperature drop are simply written as

$$\varepsilon_T = \alpha \Delta \tilde{T} \tag{47}$$

On the other hand, the relationship of the mechanical stresses and strains generated by applying only the mechanical loading to the surface can be written as

$$\sigma_M = Q \varepsilon_M \tag{48}$$

The residual stresses and strains of the full-circled rotor, each denoted by σ_R and ε_R, are then obtained by superposing stresses and strains in Eqs. (47) and (48) and :

$$\sigma_R = \sigma_M; \quad \varepsilon_R = \varepsilon_M + \alpha \Delta \tilde{T} \tag{49}$$

Since the split of the specimen causes the stress-free boundary conditions at the cutting surface, cutting the specimen in the radial direction is mechanically equivalent to applying the negative of the circumferential components of the residual stresses to the radial surface. In other words, the residual strains ε_M are released and measured on mechanical split of the specimen.

The simple but effective superposition justifies the usefulness of the split method for measuring the residual strains and stresses accumulated in the thick-walled rotor made of composite materials. Notice that, in the case of the hybrid composite rotor, the stresses and strains of the free-edged specimen caused by the temperature drop should be

calculated using a finite element method since this case is no longer axisymmetric. For completeness, each step is verified using three-dimensional finite element methods. The total residual stresses and strains can be always calculated by the stress analysis described in the previous section.
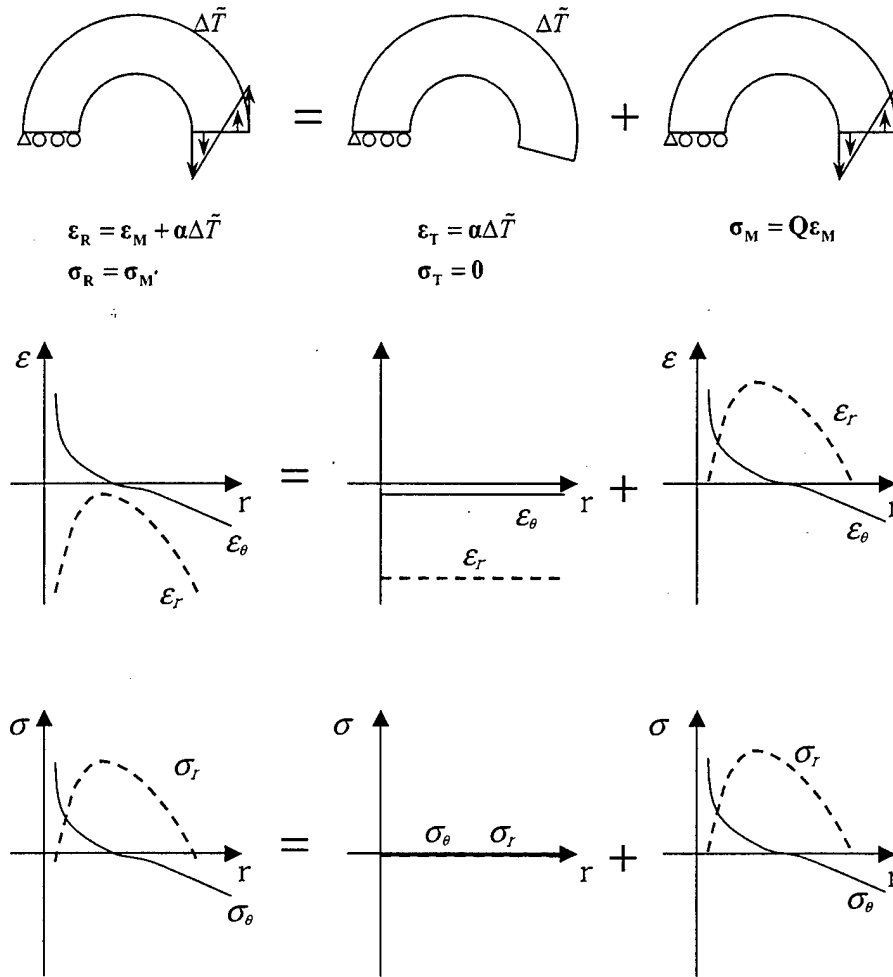

$$\varepsilon_R = \varepsilon_M + \alpha\Delta\tilde{T}$$
$$\sigma_R = \sigma_M.$$

$$\varepsilon_T = \alpha\Delta\tilde{T}$$
$$\sigma_T = 0$$

$$\sigma_M = Q\varepsilon_M$$

Figure 10. The residual stresses and strains developed inside the circular rotor are superposition of those by the stress-free temperature drop plus those by the mechanical loadings applied to the cut surface.

5.4 Measurement of Residual Strains

The composite materials are ideal for the flywheel rotor since the stresses generated by the rotational centrifugal forces can be effectively supported by the anisotropic materials. On the other hand, however, the anisotropic coefficients of thermal expansion differing in the radial and circumferential directions inevitably generate the residual strains proportionally to the temperature drop. In addition, the distribution of these residual strains is affected by the dimensional size and the stiffness anisotropy. These can be well observed in the previous section. Most importantly, understanding size effects on the residual strains is critical in design of the flywheel rotor made of composite materials.

To validate the effective temperature change presented in the previous section, the residual strains were experimentally measured for three different outer radii of 77, 110.5, 152.5 mm with the same inner radii of 37.5 mm and the length of 25.4 mm; each specimen is denoted respectively by specimen A, B, and C. The aluminum mandrel of outer and inner radii of 32.5 mm and 27.5 mm respectively were first machined with two side circular plates of the outer radius of 150 mm and the thickness of 10 mm attached for guiding the winding fiber to produce the rotor of length of 200 mm, as shown Figure 11. Resin system was prepared by mixing epoxy, catalysis and accelerator with the mass fraction ratio of 60:35:5. During the filament winding process, graphite Fibers of T300-6K, followed by dipping in the resin bath, were wound with the fiber tension of 10 N onto the mandrel rotating with the revolution speed of 50 rpm. The nose which fed the fibers axially traveled at the speed of 1m/min. Filament winding process was then followed by curing in the autoclave with the cure cycle as shown in Figure 12. In order to ensure the axisymmetric material properties, the one end of the horizontal mandrel shaft was connected to the motor and revolved with the rotational speed of 15 rpm during the whole curing process. Once cure was completed, the rotor was spliced and machined, yielding the length of 25.4 mm.

In order to assure the quality of the cylinder, the fiber volume fractions are measured along the radial direction as shown in Figure 13a. The distribution of the fiber volume fractions along the radial direction are shown in Figure 13b, and the average

fraction is 68%. Photomicrographs of the cross-sections are shown in Figure 13c.

Two sets of strain gages in the radial direction, each for radial and circumferential strains, were then glued on the one side surface of the rotor as shown in Figure 14. Each set consisted of from 3 to 15 stain gages depending on the size of the rotors. The residual stresses were released by the split ring method, that is, cutting D-section out of the rotor. The readouts before cutting the D-section were set to zero, and then recorded again after cutting. Note that the mechanical residual strains are opposite in sign of those recorded upon cutting. These values from the strain gages for each size of rotor are shown in Figure 15: the measured radial and circumferential strains of the specimens A, B, and C are represented by solid dots as shown in (a) through (f), respectively. Whereas the radial and circumferential strains of the specimen A are continuously distributed along the radius, the abrupt changes are characteristic of the strains of the specimens B and C. The abrupt change of the strains along the radius was not clearly understood until the stress analysis for the residual strains was performed.

The effective temperature change is found to be $140°C$ to best fit the experimental data in the specimen A as shown in Figure 15. The material properties used in the calculation are from those for T300/Epoxy. It is found that the temperature drops less than $140°C$ for the specimens B and C cause the delamination in the radial direction. This is manifested in Figure 16: the radial and circumferential stresses of the specimen A, B, and C with the temperature drop of $140°C$ are calculated and respectively shown in solid lines in Figure 16(a)~(f). It can be seen from Figure 16(c)~(f) that the strength ratios for the specimens B and C are beyond the value of 1 with the temperature drop of $140°C$, which means that the delamination have occurred before the temperature drop of $140°C$. The temperature drops of 93 and $82°C$ are calculated which initiate the delamination of the specimens B and C, respectively. The radial and circumferential stresses at these temperature drops are shown in dotted lines in Figure 16(c)~(f). After these delaminating temperature drops, the specimen are assumed to be split into two rings, and a further temperature is dropped, thus totally $140°C$. These consecutive residual strains of the specimen B and C are shown in solid lines in Figure 15(c)~(f). It is noticed that the damaged area experience the high radial strains and stepped aside the circumferential

strains. Even though the locations of the delamination predicted for the specimens B and C do not exactly match with those measured by the split-ring test, overall distribution of the calculated residual strains are in good agreement with the measured ones.

As a conclusion in this chapter, the residual stresses generated during the elevated temperature cure of thick section polymer composite components can lead to delamination. The purpose of this research was to gain a better understanding of residual strains in a simple way, and develop methods for measuring and predicting them. These could then be used to investigate ways to manage residual stresses in order to reduce the residual stresses and stains. Including the contact between the mandrel and rotor does change the results, but low enough to be neglected.
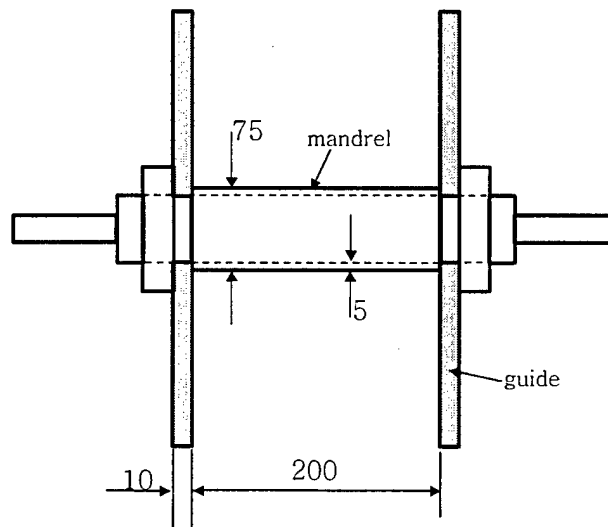
Figure 11. Mandrel with two guide plates for filament winding
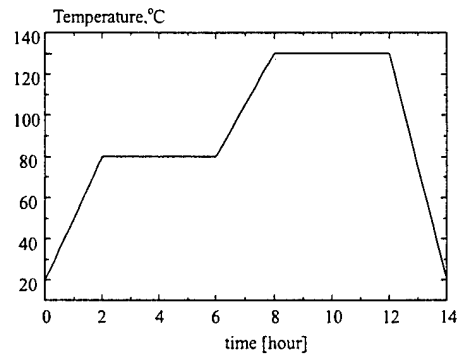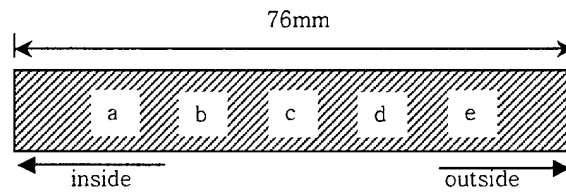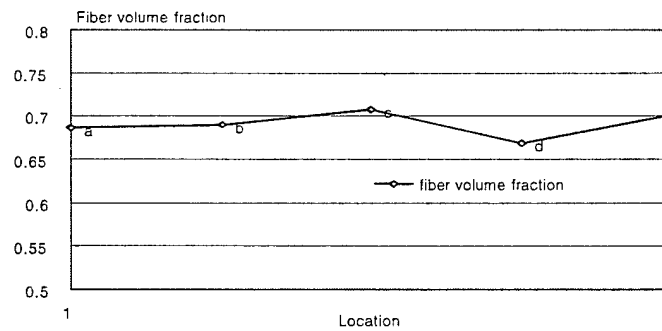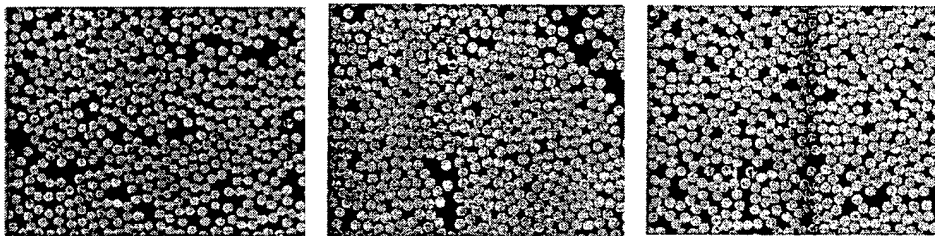
Figure 12. Two step cure cycle for specimens A, B, and C

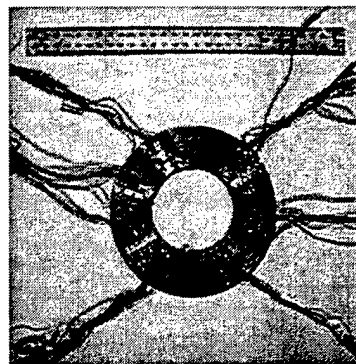(a) radial locations for measurement of the fiber volume fractions

(b) distribution of the fiber volume fractions along the radial direction
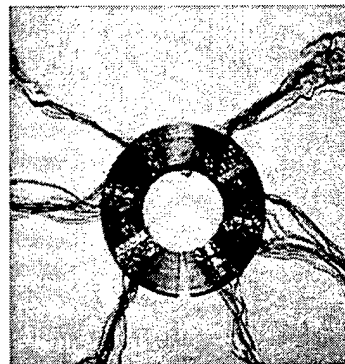

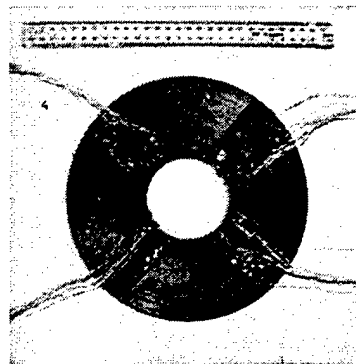(c) photomicrographs of the cross-sections a, c and e

Figure 13. Measurement of the fiber volume fraction along the radial direction
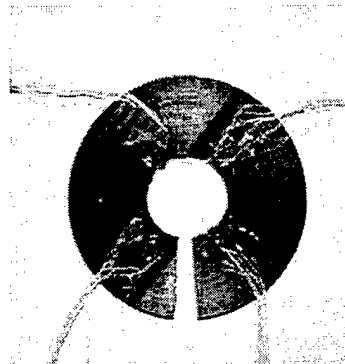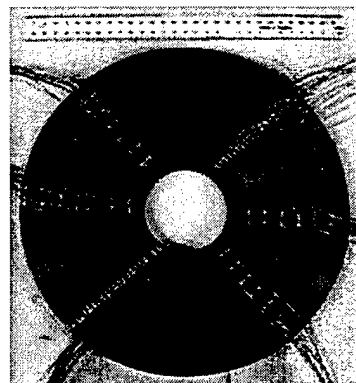
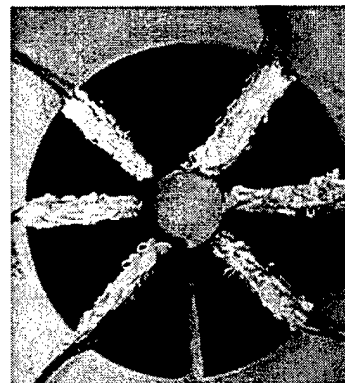(a) Specimen A before split (b) Specimen A after split

(c) Specimen B before split (d) Specimen B after split
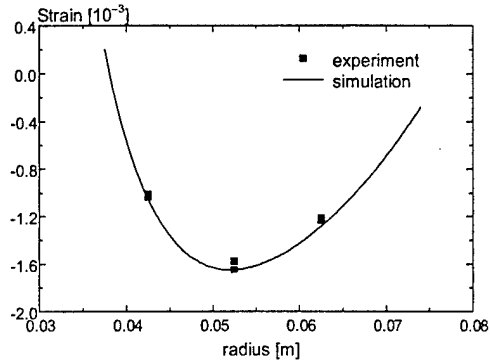
(e) Specimen C before split (f) Specimen C after split

Figure 14. Three specimens A, B and C before and after split in the split-ring test; the stresses-released strains are measured.

(a) radial strain of Specimen A
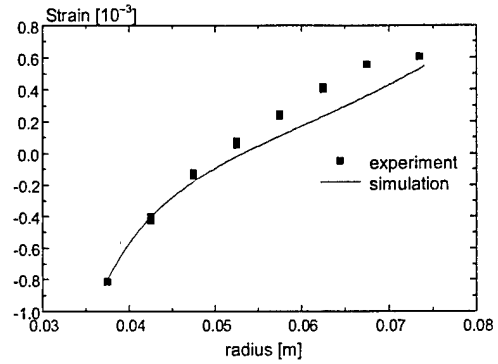
(b) hoop strain of Specimen A
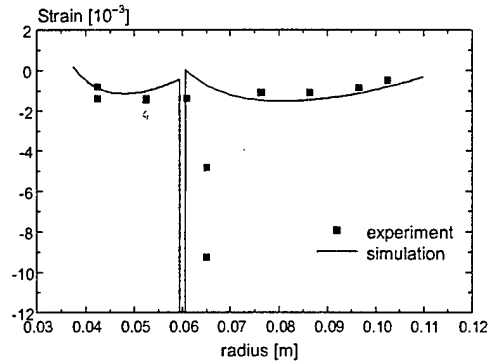
(c) radial strain of Specimen B

(d) hoop strain of Specimen B
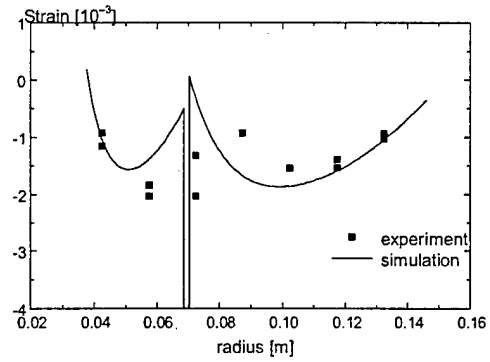
(e) radial strain of Specimen C
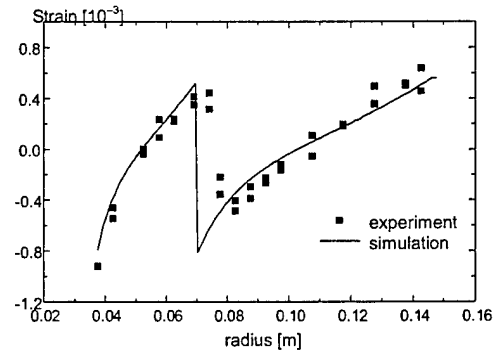
(f) hoop strain of Specimen C

Figure 15. Residual radial and circumferential strains for specimens A, B, and C measured by the split-ring test and predicted by the present methods, each denoted by the square dots and solid lines.

37
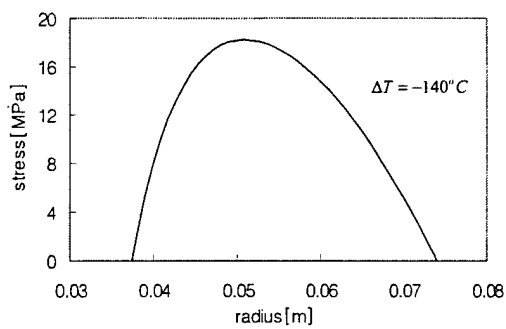
(a) radial stress of Specimen A
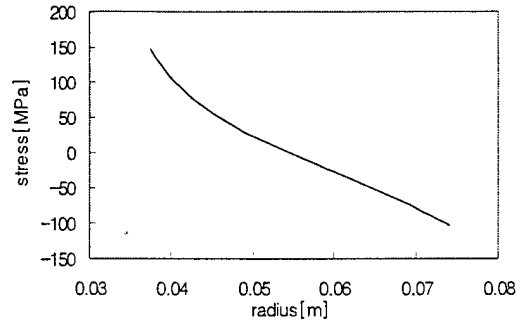
(b) hoop stress of Specimen A
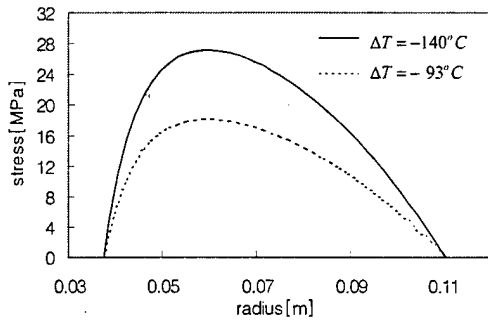
(c) radial stress of Specimen B
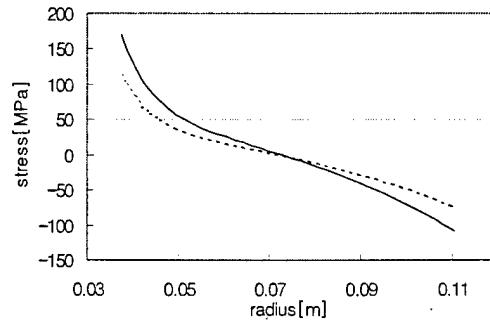
(d) hoop stress of Specimen B
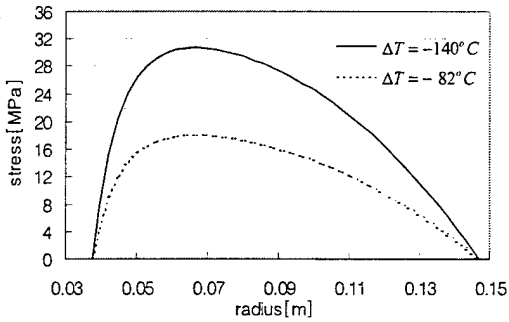
(e) radial stress of Specimen C
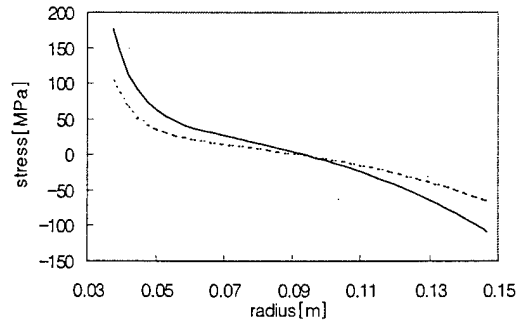
(f) hoop stress of Specimen C

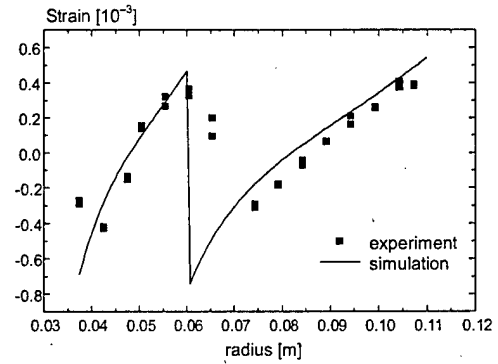Figure 16. Radial and hoop stresses of specimens A, B, and C: the dot lines for initiation of the delamination (ΔT_{d_σ} =-93$^{\circ}C$ for B and ΔT_{d_σ} =-82$^{\circ}C$ for C) and the solid lines for the effective temperature drop ΔT =-140$^{\circ}C$ without a consideration of delamination.

38

5.5 Summary

The process-induced residual strains can lead to delamination within a thick wound composite cylinder. Especially in the case of the flywheel rotor, the residual radial stresses add to those generated by the centrifugal forces, which significantly deteriorate the performance of the rotor since the radial tensile stresses are mostly sustained by the relatively weak matrix. The process-induced residual strains should be thus properly considered in design of the thick wound composite cylinders. However, a detailed universal rheological model including cure shrinkage as well as thermal strains, the process of gelation, cure kinetics, the exotherm and interaction between the rotor and the mandrel would be very difficult to set up for design of the thick wound composite rotor.

The program WINDTHICK has been used to generate the residual strains and it has been shown that the main factors influencing the residual stresses in the thick wound cylinder are mainly due to the temperature change and the chemical shrinkage. A simple stress analysis with an effective temperature change is then proposed which efficiently predict the process-induced residual stresses. In this way, the stress analysis can be effectively linked to an optimal design of the thick wound cylinders with a consideration of the process induced residual strains. Split ring tests have been performed to measure the residual strains within the thick wound cylinders of different sizes. The measured data are in good agreement with the results by the present analysis.

6. OPTIMIZATION COMPUTER CODE – FLYOPT

A proper combination of composite materials for the rotor could reduce the stress distribution in the rotor and eventually increase TSE. The objective of this study is to maximize TSE of a hybrid flywheel rotor without any material failure. Strength ratio R is used for failure analysis, where a value of R greater than 1 indicates material failure [8]. To ensure the rotor against any material failure, in this approach, strength ratio R and the damage indices D_σ and D_ε calculated at any point of the rotor must have values less than 1. The inner radius r_1 and height h of the rotor are given and the thickness t_m of each rim $(m=1,2,3,...,M)$ is used as the design variables. The optimization is then formulated as follows:

$$\textbf{Find} \quad t_m \quad (m=1,2,3,\cdots,M)$$

$$\textbf{Maximize} \quad E = \frac{1}{2}I\omega^2 \tag{50}$$

$$\textbf{Subject to} \quad \text{Max } R, D_\sigma, D_\varepsilon < 1$$

where I is a mass moment of inertia of the hybrid rotor, and ω is a rotating speed. The total stored energy (TSE) E can be thus written in terms of the inner radius r_m and outer radius r_{m+1} of each m-th rim:

$$E = \frac{\pi}{4}h\omega^2 \sum_{m=1}^{M} \left(r_{m+1}^4 - r_m^4\right)\rho_m \tag{51}$$

where the subscript m indicates each rim and the other variables include the length of the rotor h, and the density of the m-th rim ρ_m.

In order to solve the nonlinear optimization problem formulated in Eq. (50), the modified method of feasible directions for constrained minimization is used. The main task in the optimization method is to find a usable-feasible search direction and the one-dimensional search. In the every iteration of optimization, stress and strength analysis are performed and the maximum strength ratio in each ring is evaluated as described below.

40

An optimal design of a hybrid composite rotor, by maximizing TSE without any material failure as formulated in Eq. (50), is performed using a combination of composite materials with different fiber types: (A) Glass/Epoxy, (B) T300/2500, (C) T800H/2500. Optimizations are performed combining up to three different composite rims and can thus be grouped into 3 categories. In the first category, only one material is used, and in the second category, two materials, and so on. In each category only several cases of material selections and sequences are considered because it is efficient way of increasing TSE to arrange softer materials in the inner side and stiffer materials in the outer side of the rotor. The thickness of each composite rim is considered as a design variable and equally divided into element rings, resulting in a total of 30 element rings. The initial thickness for each composite rim is 20 mm, and the inner radius of the rotor is 50mm. The value for the rotating speed is taken as 60,000 RPM.

All the calculated optimum TSE are shown in Figure 17 where each bar indicates the location of each rim and thus the length of the bar means the thickness of each rim. As noted in the stress distribution, the effects of the curing temperature on the optimal design are significant. For instance, the results of the optimal designs using the material sequence A-B-C show that TSE reduces by about 30% with $\Delta \tilde{T} = -110\,℃$ and 36% with $\Delta \tilde{T} = -125\,℃$. In other words, neglecting the residual stresses may leads to causing the higher stresses than expected in the process of operating the flywheel rotor. The distributions of the strength ratios for $\Delta \tilde{T} = 0\,℃$, $\Delta \tilde{T} = -110\,℃$ and $\Delta \tilde{T} = -125\,℃$ are shown in Figure 6. It is noted that the maximum TSE is obtained when the strength ratio $R=1$ is reached in every composite rim. Thus, strength is not wasted in each rim which otherwise experience proportionately smaller stress levels. This means that maximizing TSE is equivalent to incorporating the highest possible stresses that satisfy the equilibrium and compatibility conditions. At the optimum state, each thickness of the rim is thus determined so that the strength ratio $R=1$ is reached in every composite rim. It can be obviously noted that the number and sequence of materials are very important in maximizing TSE or minimizing the stresses inside the materials. The stress distributions are effected by the sequence of stiffness, mostly hoop directional Young's modulus. Softer materials inside of the rotor, which are easier to expand in the radial direction, and stiffer materials outside of the rotor, which experience less radial displacement,

41

eventually reduce the radial stresses.

A computer program FLYOPT is developed using Microsoft Excel user-interface. The input data in blue and the output data in red for the stress analysis and the user-interface for the optimization are respectively shown in Figures 18 and 19. The design variables in the optimization module can be linked to any variables in the stress analysis module.
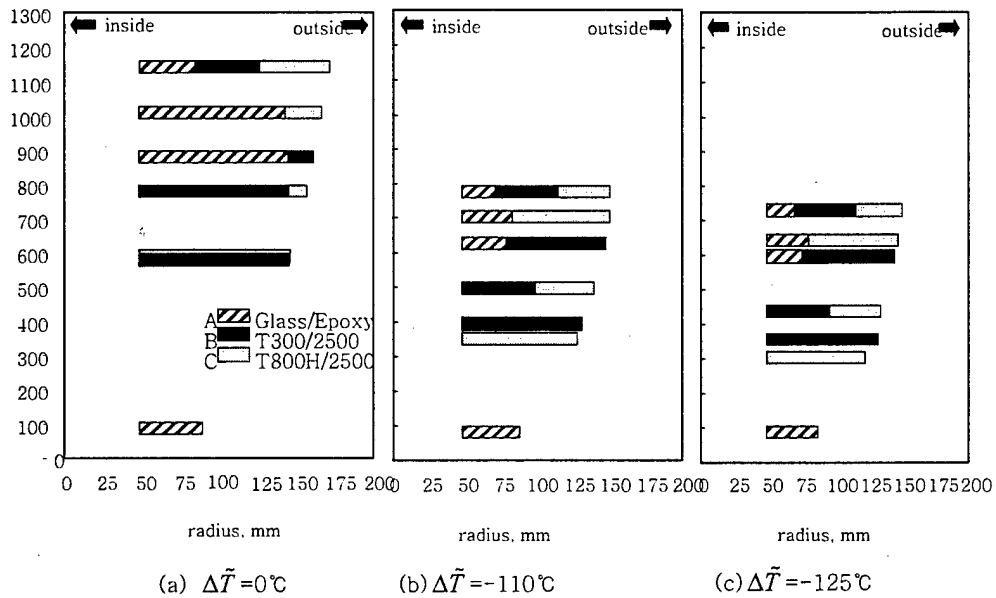

Figure 17. Comparison of optimal thickness of composite rims and the corresponding TSE (Wh) for various selections of composite material (ω=60,000RPM).

INPUTS in Blue

w (RPM)	65392
Max w (RPM)	65392
Min w (RPM)	32696
Length	0.0254
R_i :	0.0095
R_o :	0.0762
R_m:	0.0095
Total_Thickness	0.0667
Nel :	150

plane-option; 0 for PSr	2
Solution Type	GPs

Hybrid Rings	Mandrel	Group_1	Group_2	Group_3	Group_4
Material Group Numb	0	1	2	3	4
Material_Number	11	11	11	11	11
Material_Thickness	0	0.003175	0.00635	0.009525	0.009525
Material_Name	Scotch[SI]; vf=0.65	tch[SI]; vf=0.65	tch[SI]; vf=0.65	tch[SI]; vf=0.65	tch[SI]; vf=0.65
Number_of_Rings	0	20	20	20	20
Material_Angle	0	0	0	0	0
Material_temp_Curre	25	25	25	25	25
Material_dT	25	25	25	25	25
Material_chemical_sh	0	0	0	0	0
Material_Group	0	20	40	60	80

RESULTS in Red

Ip (Kg*m2)	0.00277842	Mass (Kg)	0.94	Volume (liter)	0.456093736
E_max (Wh)	18	E_min(Wh)	5	E_usable	14
SED_max (Wh/Kg	19.20	SED_min(Wh/Kg	4.80	SED_usable(Wh/	14.4028545
SVED_max (Wh/liter	39.68	SVED_max(Wh/l	9.92	SVED_usable(W	29.75629739
Tip Speed (m/sec)	521.8049681	Inner Speed (m/se	65.22562101	Cost_material (S)	2.768032882

Failure Analysis	Sig_theta/X,MAX	Sig_theta/X,MIN	Sig_z/Y, Max	Sig_r/Y, Max	Tsai-Wu
Winding	0.00000	0.00000	0.00000	0.00000	0.00000
Winding_Curing	0.00263	-0.00567	-0.00570	-0.03572	0.01431
Mandrel_Removed	0.00263	-0.00567	-0.00570	-0.03572	0.01431
Rotating at w	0.18664	0.04569	-0.26254	1.11899	0.97495
RPM_burst	151765		128032	61898	66237
E_burst (Wh)	97.47		69.37	16.21	18.57
SED_burst (Wh/Kg)	103.44		73.62	17.21	19.70
CSED_burst(Wh/S)	35.21		25.06	5.86	6.71

Figure 18. Input data and output results in the stress module of the program FLYOPT for the flywheel rotor subjected to both the thermal changes and the rotational speed.

Parameters in the Calling Stat	
Optimization N	1
MinMax	0
IGRAD	0
NDV	8
NCON	0

Objective	974.950

	Design Variables , X(I)			Constraints	
Dindex	Lower Bound	X(I)	Upper Bound	Cindex	Constraint<0
1	0	29.45345688	90	0	-0.025050225
2	0	22.64533806	90	0	0.0001
3	0	15.73644066	90	0	
4	0	0	90	0	
5	0	0	90	0	
6	0	0	90	0	
7	0	0	90	0	
8	0	0	90	0	
0				0	
0				0	

Figure 19. The design variables, the constraints, and the objective functions specified in the optimization module of the program FLYOPT.

43

7. CONCLUSIONS

The goal of the present work is to develop an optimization tool for a design of the flywheel rotor with a consideration of the process-induced residual strains accumulated during the winding and curing process. A stress analysis of a helically wound hybrid rotor is developed in which an equivalent temperature change is used to consider the residual stresses and strains. The validity of the stress analysis has been proved using a three-dimensional finite element program. The effects of the material hybridization and the helical winding angles on the thermal stresses are also investigated. A WINDTHICK program is also used to validate an effective temperature change considered in the analysis. The residual stresses have been experimentally measured using a split-ring test. As a product of this work, a computer program for the optimum design of the hybrid composite flywheel rotor are developed which covers the various size and material properties of the rotor.

REFERENCES

[1] Anerdi G, Brusaglino G. Technology Potential of Flywheel Storage and Application Impact on Electric Vehicles. *12th International Electric Vehicle Symposium (EVS-12)* 1994;1:37-47.

[2] Christopher DA, Beach R. Flywheel Technology Development Program for Aerospace Applications. *IEEE AES System Magazine* 1998;13(6):9-14.

[3] Rodriguez GE, Studer PA, Baer DA. Assessment of Flywheel Energy Storage for Space Craft Power System. *NASA Technical Memorandum 85062*, 1983.

[4] Genta G. Kinetic Energy Storage. London: Butterworths & Co., Ltd., 1985.

[5] Grudkowski TW, Meyer TG, Wawrzonek PH. Flywheels for Energy Storage. *SAMPE Journal* 1996;32(1):65-69.

[6] Post RF, Fowler TK, Post SF. A High Efficiency Electromechanical battery. *Proceedings of the IEEE* 1993;31(3):462-474.

[7] Danfelt EL, Hewes SA, Chou TW. Optimization of composite flywheel design. *International Journal of Mechanical Sciences* 1977;19:69-78.

[8]   Ha SK, Jeong HM, Cho YS. Optimum Design of Thick-walled Composite Rings for an Energy Storage System. *Journal of Composite Materials* 1998;32(9):851-873.

[9]   Ha SK, Yang HI, Kim DJ. Optimal Design of a Hybrid Composite Flywheel with a Permanent Magnet Rotor. *Journal of Composite Materials* 1999;33(16):1544-1575.

[10] Ha SK, Kim DJ, Sung TH. Optimum Design of Multi-ring Composite Flywheel Rotor Using a Modified Generalized Plane Strain Assumption. *International Journal of Mechanical Sciences* 2001; 43: 993-1007.

[11] Guemes JA. Curing Residual Stresses and Failure Analysis in Composite Cylinders. *Journal of Reinforced Plastics and Composites* 1994;13(5):408-419.

[12] Hjellming LN, Walker JS. Thermal Curing Cycles for Composite Cylinders with Thick Walls and Thermoset Resins. *Journal of Composite Materials* 1989;23(10):1048-1064.

[13] Bogetti TA, Gillespie JA. Process-Induced Stress and Deformation in Thick-Section Thermoset Composite Laminates. *Journal of Composite Materials,* 1992; 26(5):626-660.

[14] LEE SY, Springer GS. Filament Winding Cylinders: I. Process Model. *Journal of composites materials* 1990;24(12):1270-1298.

[15] Calius EP, LEE SY, Springer GS. Filament Winding Cylinders: II. Validation of the Process Model. *Journal of composites materials* 1990;24(12):1299-1343.

[16] LEE SY, Springer GS. Filament Winding Cylinders: III. Selection of the Process Variables. *Journal of composites materials* 1990;24(12):1344-1366.

[17] Cai Z, Gutowski T, Allen S. Winding and Consolidation Analysis for Cylindrical Composites Structures. *Journal of composites materials* 1992;26:1374-1399.

[18] Herakovich CT, Tarnopol'skii YM. Structures and Design; Handbook of Composites Vol. 2, Amsterdam: Elsevier Science Publishers B.V., 1989, p. 531-582.

[19] White SR, Zhang Z. The Effect of Mandrel Material on the Processing-Induced Residual Stresses in Thick Filament Wound Composite Cylinders. *Journal of Reinforced Plastics and Composites* 1993;12(6):698-711.

[20] Ganley JM, Maji AK, Huybrechts S. Explaining Spring-In in Filament Wound Carbon Fiber/Epoxy Composites. *Journal of Composite Materials* 2000;34(14):1216-1239.

45

[21] Garbys CW, Bakis CE. Simplified Analysis of Residual Stresses in in-situ Cured Hoop-Wound Rings. *Journal of Composite Materials* 1998;32(13):1325-1343.

[22] Serif MA, Kishaway HA. Determining Residual Stresses in Thin-Walled Ceramic/Ceramic Composite Pipes. *Journal of American Ceramic Society* 1999; 82(4):977-980.

[23] Peri M. An Improved Split-Ring Method for Measuring the Level of Autofrettage in Thick-Walled Cylinders. *Journal of Pressure Vessel Technology, ASME* 1998; 120(2):69-73.

[24] Lekhnitskii SG. Anisotropic Plates. New York: Gordon and Breach Science Publishers Inc., 1968.

[25] Tsai SW. Composites Design. Dayton, Ohio: Think Composites, 1988.

[26] Ha SK, Yoon YB, Han SC. Effects of Material Properties on the Total Stored Energy of a Hybrid Flywheel Rotor. *Archive of Applied Mechanics* 2000;70:571-584.